Developing novel diffusion MRI methods for comprehensive analysis of restricted and anisotropic self-diffusion system

Jiang, Hong

2023

Document Version:
Publisher's PDF, also known as Version of record

Developing novel diffusion MRI methods for comprehensive analysis of restricted and anisotropic self-diffusion system

HONG JIANG | DIVISION OF PHYSICAL CHEMISTRY | LUND UNIVERSITY

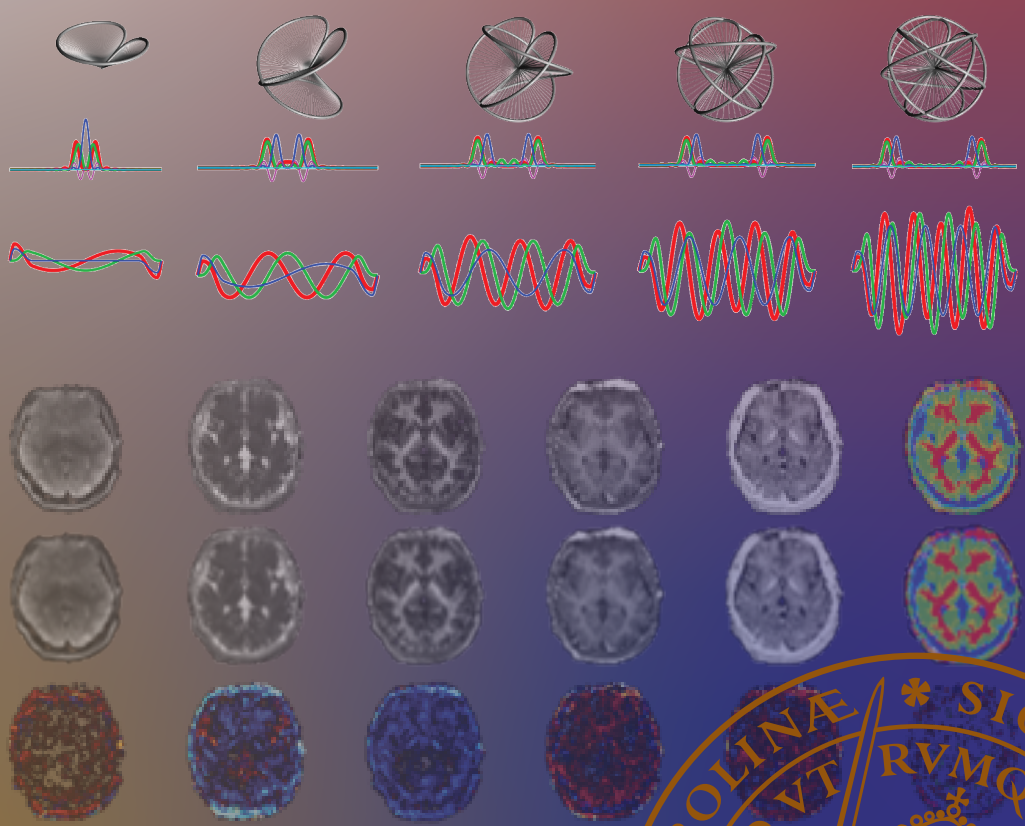

Developing novel diffusion MRI methods for comprehensive analysis of restricted and anisotropic self-diffusion system

Developing novel diffusion MRI methods for comprehensive analysis of restricted and anisotropic self-diffusion system

Hong Jiang

LUND
UNIVERSITY

DOCTORAL DISSERTATION

Doctoral dissertation for the degree of Doctor of Philosophy (PhD) at the Faculty of Science at Lund University to be publicly defended on the 29th of September 2023 at 09:15 in Lecture Hall B, Department of Physical Chemistry, Lund University，Naturvetarvägen 14, Lund, Sweden

Faculty opponent
Associate Professor, John Georg Seland
Department of Chemistry, University of Bergen, Norway

Organization: LUND UNIVERSITY

Document name: DOCTORAL DISSERTATION

Date of issue: 2023-09-29

Author(s): Hong Jiang

Sponsoring organization:
China Scholarship Council,
No. 201807930011

Title and subtitle: Developing novel diffusion MRI methods for comprehensive analysis of restricted and anisotropic self-diffusion system

Abstract:

Diffusion MRI is a non-invasive imaging technique used to study the microstructural properties of biological tissues by observing the self-diffusion of water molecules. Traditional diffusion MRI methods, based on the pulsed gradient spin-echo sequence, employ magnetic field gradients to encode information about translational motion. However, this approach combines various aspects of diffusion, such as restriction, anisotropy, and flow, into a single observable, leading to interpretation ambiguities, especially in complex heterogeneous materials like living biological tissues.

In this thesis, we address these challenges and push the boundaries of diffusion MRI by introducing innovative techniques for studying biological tissue microstructure. Our approach centers around the "double-rotation" technique borrowed from solid-state NMR, which generates modulated gradient waveforms, enabling us to explore the 2D frequency-anisotropy domain in-depth. By integrating this technique with oscillating gradients and tensor-valued encoding, we create a comprehensive methodology for data acquisition. Drawing inspiration from the "model-free" analytical strategies originally designed for studying rotational dynamics in macromolecules, we extend its applicability to MRI techniques for understanding diffusion in biological tissues.

Through a series of proof-of-principle experiments, we validate our novel acquisition and analysis strategy across various samples. These experiments encompass the study of isotropic and anisotropic Gaussian diffusion in simple liquids, characterizing anisotropic Gaussian diffusion in a lyotropic liquid crystal with lamellar microstructure, and exploring restricted diffusion in a yeast cell sediment. Additionally, we showcase the effectiveness of our methods on ex vivo mouse brain and tumor tissue, highlighting the practical potential of our approach.

Our proposed double-rotation gradient waveforms enable comprehensive sampling of both the frequency and "shape" dimensions of diffusion encoding, providing detailed insights into restriction and anisotropy in heterogeneous materials. The implications of our work extend to model-free investigations, allowing us to understand microstructural changes linked with pathology or normal brain development.

Key words:

NMR, MRI, restricted diffusion, anisotropic diffusion, diffusion encoding, q-vector, diffusion spectrum, encoding spectrum, tissue microstructure, heterogeneity

Classification system and/or index terms (if any)

Supplementary bibliographical information

Language: English

ISSN and key title:

ISBN: 978-91-7422-978-3 (print)
978-91-7422-979-0 (pdf)

Recipient's notes

Number of pages: 216

Price

Security classification

Developing novel diffusion MRI methods for comprehensive analysis of restricted and anisotropic self-diffusion system

Hong Jiang

LUND
UNIVERSITY

Coverphoto by

Copyright Hong Jiang

Faculty of Science

Physical Chemistry

ISBN 978-91-7422-978-3 (print)

978-91-7422-979-0 (pdf)

Printed in Sweden by Media-Tryck, Lund University

Lund 2022

Dedicated to my family

Table of Contents

Acknowledgements

I would like to take this opportunity to express my heartfelt gratitude to all those who have played a significant role in helping me complete this thesis. Without your support, this journey would not have been possible.

First and foremost, I am grateful to my supervisor **Daniel Topgaard** for providing me with the opportunity to work on my Master's thesis in your research group during the spring of 2018. This experience allowed me to engage in an interesting research project and later pursue my Ph.D., a journey that spanned nearly six years. Your continuous support, valuable advice, and mentorship have contributed significantly to finish the journey of my Ph.D.

I extend my thanks to my co-supervisors **Samo Lasič** and **Dan Lundberg** for their help. **Samo Lasič**, thank you for your kind assistance and fruitful discussions on diffusion MRI. **Dan Lundberg**, I am deeply grateful for the guidance you provided in sample preparation and the use of the light microscope, which facilitated our search for the desired samples.

A special appreciation goes to **Göran Carlström** for assisting me in changing the probe and setting up the NMR instrument.

I also want to acknowledge the contributions of all the current and former members of the NMR group, including **Sarah Mailhiot**, **Alexis Reymbaut**, **Linn Thrane**, **Jan Martin**, **Maxime Yon**, **Simon Fridolf**, **and Kenneth Pak Or**, special thanks to my co-authors, especially **João Martins**, **Chantal M. W. Tax**, and **Leo Svenningsson**, with whom I thoroughly enjoyed discussing NMR-related topics.

My sincere gratitude goes to all the members of the Physical Chemistry Division for creating a pleasant work environment. **Ulf Olsson** and **Anna Stradner**, thank you for helping me plan my Ph.D. journey. I am also thankful to **Maria Lövgren**, **Maria Södergren**, **Christopher Ward** and **Peter Holmqvist** for ensuring everything ran smoothly. I cherish the enriching discussions with colleagues during our PhD seminars and coffee breaks.

Furthermore, I want to express my gratitude to **Mohammad Arif Kamal**, **Antara Pal**, **Quoc Dat Pham, Meina Wang**, **Xiaoyan Liu**, **Guanqun Du**, **Meiting Wang**, **Junhao Dong**, **Jing Hu and Runtian Qie**， my KC buddies. I am delighted to have shared my joys and frustrations in life and work with all of you. Thank you, my friends. Your presence has made me feel less lonely while being far away from home, especially during challenging times like the pandemic. Your companionship has been particularly important to me.

To all my friends whom I have met in Sweden, over the course of ten years, I have made many like-minded friends. Among them are those whom I have known since I first arrived here over a decade ago—**Xuan** (璇璇), **Ruiyu** (芮羽), **Xiaoting** (晓

婷), **and Hui**(慧姐). You have always provided me with the warmest help whenever I felt most helpless.

I am also grateful for the company of fellow moms, including **Ruiyu**(芮瑜), **Mengqin**(梦琴), **Fei**(谢菲), **Ka**(卡卡)， **Amber**（之杨)， **Xiaohan**(晓菡)， **Fangfang**(芳芳), **Zhen**(李贞), **Kena**(柯娜)， **Xinai**(新媛), and **Zhiyi**(智一), who have been together with me in the journey of raising children. I am especially thankful to **Xiaokang**(晓康) and **Gloria**, who accompanied me through the most challenging times of the pandemic. Your positive and optimistic attitudes have been a source of inspiration during my lowest moments. Together, we studied and cooked at home, and those days during the dark period of the pandemic are the ones I often think back to.

Lastly, I want to give a special thanks to my family. To **my parents**, your trust and care have been unwavering, supporting me in every decision I made. To **my sisters**, who took on the responsibility of caring for our parents in my absence, you have been my pillars of strength. I am grateful to **my parents' in-laws** for their help in taking care of our children over the years, without which I could not have completed my doctoral studies. To my children (**William Si Chang** and **Richard Xing Chang**), your presence fills my life with happiness despite the challenges of juggling parenthood and thesis writing. Whenever I return home exhausted, your smiles and hugs make me feel like the luckiest person alive.

我要特别感谢我的家人。我的父母，你们一直信任和关心我，永远支持我做出的任何决定。谢谢我的姐姐和妹妹，在我远离家乡的这么多年，你们分担了照顾父母的任务，你们是我坚强的后盾。谢谢我的公公婆婆，感谢你们这么多年来一直帮忙照顾孩子，如果没有你们的帮助，我无法想象我能完成我的博士学业。

Finally, and most importantly, I want to express my deepest gratitude to my husband (**Zhiwei**). My dear husband, you are the only one person in this world with whom I can share every detail of my life and discuss NMR. Your continuous encouragement, assistance, understanding, and unwavering support have been the bedrock of my journey. Your presence brings me comfort, especially during moments of uncertainty and difficulty.

Once again, to all of you who have been part of this journey, thank you from the bottom of my heart. Your contributions have been immeasurable, and I am forever thankful for your support.

Hong Jiang

姜虹

Popular summary in English

Unlocking the mysteries of brain imaging: A Journey into the world of diffusion MRI

This thesis explores the fascinating world of diffusion magnetic resonance imaging (MRI), a non-invasive technique that allows us to observe inside our brain and understand the structure of biological tissues. However, traditional approaches have limitations, blurring the picture due to overlapping movements of water molecules.

The thesis introduces an exciting development by adopting a new approach that provides a clearer and more detailed view of the microscopic processes within our brain. You can think of it as switching from a blurry old TV set to a new, high-definition screen.

Drawing inspiration from a technique called solid-state Nuclear Magnetic Resonance (NMR), commonly used in material and chemical studies, this thesis introduces a novel approach. It is like borrowing techniques from one field and applying them to another. The goal is to improve our understanding of the microscopic processes happening inside our brain.

Up until now, research has primarily focused on two types of diffusion: restricted diffusion, which changes with time, and Gaussian anisotropy diffusion, which does not change with time. To dive deeper into these processes, the thesis presents a method called the "double-rotation" technique. This unique approach generates a special pattern in MRI signals, allowing us to explore both restricted and anisotropic water molecule movements in unprecedented detail. But that is not all. The thesis also combines analysis strategies, called "model-free" approach from studying how large molecules move and rotate, to diffusion MRI. When we combine the data-collecting "double-rotation" technique and the data analysis "model-free" approach, we get information about how tiny parts in our tissues are arranged. This special way we use is a big leap forward for diffusion MRI. It's like finding a treasure map that leads us to learn a lot about complicated things, like the inside of healthy brains and tumors.

The PhD thesis is like a guide to a super exciting adventure that takes us on a journey where things we only saw in movies are actually happening. We use the power of diffusion MRI to peek inside our brains and learn amazing things. By borrowing secrets from different areas of science, we are exploring new places in brain imaging, getting closer and closer to uncovering the hidden stories of our most important organ.

List of Papers

This thesis is based on the following publications:

Paper I: Lamellar liquid crystal phantom for validating diffusion MRI methods to distinguish oblate and prolate diffusion tensors on whole-body scanners

Hong Jiang, João P. de Almeida Martins, Dan Lundberg, Chantal M. W. Tax, Daniel Topgaard

Manuscript in preparation for NMR in Biomedicine

Paper II: Multidimensional encoding of restricted and anisotropic diffusion by double rotation of the q vector

Hong Jiang, Leo Svenningsson, and Daniel Topgaard

Magnetic Resonance, 2023, 4, 73–85

Paper III: Model-free approach to the interpretation of restricted and anisotropic self-diffusion in magnetic resonance of biological tissues

Omal Narvaez, Maxime Yon, **Hong Jiang**, Diana Bernin, Eva Forssell-Alonsson, Alejandra Sierra, Daniel Topgaard

Manuscript in preparation for Physical Review E

Paper IV: Frequency dependent diffusion: overfitting or meaningful parameter for multidimensional diffusion relaxation corelation MRI

Maxime Yon, **Hong Jiang**, Omar Narvaez, Jan Martin, Diana Bernin, Frederik Laun, Alejandra Siena, and Daniel Topgaard

Manuscript in preparation

Author's contribution to the papers

Paper I: Lamellar liquid crystal phantom for validating diffusion MRI methods to distinguish oblate and prolate diffusion tensors on whole-body scanners

I assembled samples, acquired MRI data using an NMR spectrometer, processed and analysed both preclinical and clinical MRI data. I was also responsible for writing the manuscript.

Paper II: Multidimensional encoding of restricted and anisotropic diffusion by double rotation of the *q* vector

I assembled the phantoms and acquired the data. I also contributed to develop theories and software. I took part in processing and analysing the data. Additionally, I contributed to the writing of the manuscript.

Paper III: Model-free approach to the interpretation of restricted and anisotropic self-diffusion in magnetic resonance of biological tissues

I was responsible for developing and preparing the phantoms, as well as acquiring and processing the MRI data. Additionally, I contributed to the writing of the manuscript.

Paper IV: Frequency dependent diffusion: overfitting or meaningful parameter for multidimensional diffusion relaxation corelation MRI

I was responsible for developing and preparing the phantoms. I contributed to the writing of the manuscript.

Abbreviations

ADC	Apparent Diffusion Coefficient
DDE	Double Diffusion Encoding
DOR	Double Rotation
FID	Free Induction Decay
MRI	Magnetic Resonance Imaging
MAS	Magic Angle Spinning
MSD	Mean Square Displacement
NMR	Nuclear Magnetic Resonance
PGSE	Pulse Gradient Spin-Echo
PAS	Principal Axis System
RF	Radiofrequency
SE	Spin-Echo

1 Introduction

The thesis centres around the development of a novel diffusion MRI method, including approaches for data acquisition and analysis. This method is designed to reveal intricate details about the microstructures within living tissues, with a special focus on the human brain. This section will offer an overview of the motivation, objectives for the thesis work.

1.1 Motivation

The functioning of the human brain is closely connected to its structure. This connection is impacted by multiple factors, including changes caused by pathological conditions like tumors and schizophrenia, as well as the natural development of the brain as it ages and the acquisition of knowledge. Together, these factors result in quantifiable modifications in the brain's structure across a wide range of time and size scales. It's reasonable to infer that large-scale changes are preceded by cellular-level adjustments. The structure of brain tissues can generally be observed at the cellular level by studying *ex vivo* tissues using optical or electron microscopy techniques [1, 2]. However, these methods are not suitable for studying living human subjects, there is a great need for new non-invasive tools to assess cellular level for our *vivo* tissues.

Diffusion magnetic resonance imaging (MRI) is an ideal candidate for this purpose, as it enables the non-invasive observation of the brain's morphology at the micrometer length scale and millisecond time scale [3, 4]. By measuring the self-diffusion of molecules in biological tissues, we can obtain information about microscopic structures, including the size, shape, and orientation of cells.

While conventional techniques in diffusion MRI depend on the utilization of pulsed magnetic field gradients for signal encoding [5]. This method blends various aspects of diffusion into a single observable, including time dependence restricted diffusion, anisotropic diffusion, and flow. As a result, this approach introduces uncertainties during interpretation and offers only averaged microstructural information for each voxel [6-9].

Significantly, there has been notable progress in the field of diffusion MRI in recent times. New methodologies with more advanced signal encoding have been

introduced with the aim of untangling various aspects of translational motion. Especially, there has been increased attention towards isolating restricted diffusion and anisotropic diffusion, as restricted diffusion is linked to cell sizes [10], and anisotropic diffusion is associated with cell shapes [11]. While many studies have focused on either restricted diffusion [12] or anisotropic encoding [13], a challenge emerges when dealing with heterogeneous tissues. Within each imaging voxel, there exists a variety of cell sizes and shapes. Current diffusion MRI acquisition and analysis protocols struggle to accurately extract microstructural information encompassing both cell sizes and shapes.

1.2 Thesis objective

To tackle this challenge, the thesis introduces an innovative diffusion MRI methodology. This approach enables the identification of both restricted and anisotropic diffusion within a comprehensive multidimensional framework and provides unprecedented specificity in reporting relevant microstructural properties.

The specific objectives of this project are as follows:

1. Develop a data acquisition protocol capable of detecting both restricted and anisotropic diffusion within a unified multidimensional framework.
2. Create samples that mimic the physiological environments of different microstructures in our brain for validating the newly developed data acquisition protocol.
3. Develop a data analysis method capable of processing the data collected using the newly developed data acquisition protocol.
4. Apply this novel data acquisition protocol and data analysis method to biological tissues to assess relevant microstructural properties.

In the upcoming sections, I will provide a comprehensive overview of the work presented in my thesis. This will include an introduction to the relevant knowledge of diffusion, NMR, and phantoms utilized in our study. Subsequently, I will introduce our innovative approaches, namely the double rotation encoding method and the model-free quantitative metrics. The thesis will conclude with final remarks that effectively summarize the significance and implications of the research outcomes.

2 Diffusion

Diffusion is the translational motion of molecules, which occurs in all liquids and gases. Diffusion is the process where molecules disperse due to their random movement driven by thermal energy. Molecules continually collide with each other, causing their velocities and positions to constantly change. The trajectory illustrated in Figure 2.1 provides a representation of a single particle's path in two dimensions. At any given moment, the particle possesses a specific direction and velocity, but in the subsequent moment, it undergoes a complete transformation in both aspects.

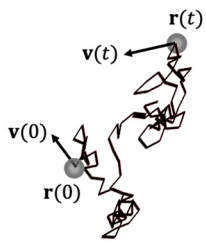

Figure 2.1: The two-dimensional trajectory of a diffusing particle. **r**(0) represents the initial position and **v**(0) represents the initial velocity. The particle's position at any given time (**r**(*t*)) and its corresponding velocity (**v**(*t*)) vary the time.

In this section, we present fundamental knowledge about diffusion, exploring the phenomenon from both macroscopic and microscopic perspectives. The section starts with an introduction to various types of diffusion, then delves into diffusion at the macroscopic continuum and microscopic molecule levels. It further discusses anisotropic diffusion and introduces the concept of the diffusion tensor.

2.1 Types of diffusion

In scientific literatures [14-17], the word “diffusion” is often used imprecisely and ambiguously because there are different types of diffusion. To clarify this, it is important to clearly define and distinguish between these various types. Diffusion can be classified into different categories based on several factors.

Self-diffusion vs. Mutual diffusion:

Self-diffusion refers to the stochastic motion of molecules due to the inherent thermal energy possessed by particles at thermal equilibrium. Mutual diffusion, also known as interdiffusion, takes place when different types of molecules or substances diffuse and mix with each other. It's the result of concentration gradients between the substances, where molecules move from regions of higher concentration to regions of lower concentration.

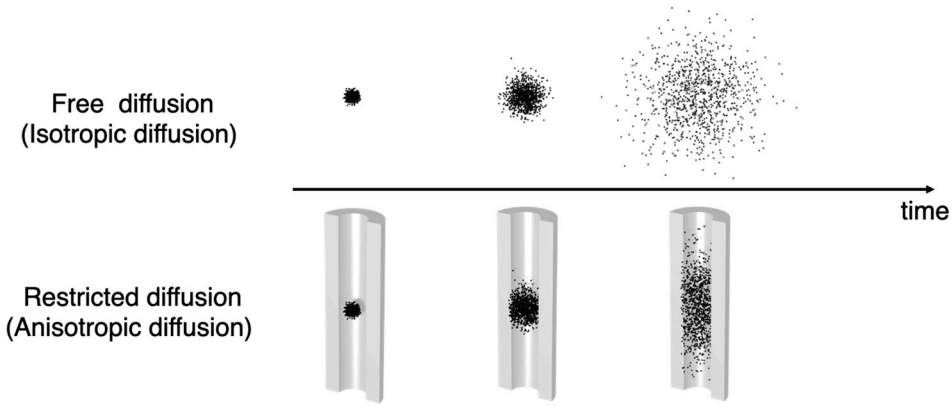

Figure 2.2: Simulated free/isotropic diffusion and restricted/anisotropic diffusion. Upper panel: Brownian dynamics simulation of a particle ensemble without boundary constraints, exemplifying free diffusion and isotropic behavior. Lower panel: Brownian dynamics simulation of a particle ensemble confined within an impermeable cylinder, showcasing restricted diffusion and anisotropic behavior [18].

Free diffusion vs. Restricted diffusion:

Free diffusion is the unrestricted random movement of molecules in a medium, where molecules can diffuse freely without encountering significant obstacles or constraints. In contrast, restricted diffusion occurs when molecules face obstacles or confinement that restrict their movement, leading to slower or hindered diffusion. Figure 2.2 shows two types of diffusion scenarios. In the upper panel, particles move freely without any boundaries, demonstrating free diffusion. In the lower panel, particles are trapped inside a cylinder, showing restricted diffusion.

Isotropic diffusion vs. Anisotropic diffusion:

Isotropic diffusion occurs when molecules diffuse uniformly in all directions within a medium, without any preferential orientation or direction. Anisotropic diffusion, on the other hand, is characterized by directional dependence, where the diffusion rate varies with different directions due to structural or geometric anisotropy of the medium. Figure 2.2 showcases these diffusion patterns visually. The upper panel features a simulation of isotropic diffusion, where particles move freely in all directions within the medium. In the lower panel, anisotropic diffusion is

represented by particles confined within a cylinder. This confinement introduces directional dependence, leading to variations in the diffusion rate based on the cylinder's geometric attributes.

In this thesis, our primary focus is on studying self-diffusion, specifically the self-diffusion of water molecules within complex microscopic materials such as biological tissues. Henceforth, we will simply refer to this as diffusion.

2.2 Exploring diffusion from macroscopic continuum approach

The study of self-diffusion can be explored from two different perspectives. First, at the macroscopic level, treating the particles as a continuous medium. Secondly, at the molecular level, which involves analysing the velocities, positions, and interparticle collisions of individual molecules. To begin, we focus on the continuum approach at the macroscopic level. Then, in section 2.3, we discuss the motion at the molecular level.

By utilizing the continuum approach and incorporating Fick's second law to derive the diffusion equation, and in conjunction with appropriate initial and boundary conditions, the concept of diffusion propagators is introduced.

2.2.1 Diffusion equation

In a macroscopic system, diffusion can be thought of as the movement of particles from regions of high concentration to regions of low concentration. Fick's first law establishes a relationship between the diffusion coefficient D and the particle flux $\mathbf{J}$ in a system with a concentration gradient $\nabla c(\mathbf{r},t)$:

$$\mathbf{J}(\mathbf{r},t) = -D\nabla c(\boldsymbol{r},t). \tag{2.1}$$

Fick's second law states that the change in concentration with respect to time $\partial c(\mathbf{r},t)/\partial t$ is equivalent to the spatial divergence of the diffusion flux $\mathbf{J}(\mathbf{r},t)$:

$$\frac{\partial c(\mathbf{r},t)}{\partial t} = -\nabla \cdot \mathbf{J}(\mathbf{r},t). \tag{2.2}$$

By substituting equation 2.2 into equation 2.1, we arrive at the diffusion equation:

$$\frac{\partial c(\mathbf{r},t)}{\partial t} = D\nabla^2 c(\mathbf{r},t). \tag{2.3}$$

2.2.2 Propagators

The diffusion propagator, denoted as $P(\mathbf{r}_0,\mathbf{r}_1,t)$, represents the probability of finding a particle initially at a position $\mathbf{r}_0$ and at a position $\mathbf{r}_1$ after a time t. It is a probability function that satisfies the normalization condition:

$$\int_{-\infty}^{\infty} P(\mathbf{r}_0, \mathbf{r}_1, t) d\mathbf{r}_1 = 1. \quad (2.4)$$

The probability density $P(\mathbf{r}_0,\mathbf{r}_1,t)$ can be seen as an ensemble-averaged concentration of probabilities for a single particle. Therefore, it is reasonable to assume that it follows the diffusion equation 2.3:

$$\frac{\partial P(\mathbf{r}_0,\mathbf{r}_1,t)}{\partial t} = D\nabla^2 P(\mathbf{r}_0, \mathbf{r}_1, t), \quad (2.5)$$

The initial condition is given by:

$$P(\mathbf{r}_0, \mathbf{r}_1, 0) = \delta(\mathbf{r}_1 - \mathbf{r}_0) = \begin{cases} \mathbf{1}, (\mathbf{r}_1 = \mathbf{r}_0) \\ 0, (\mathbf{r}_1 \neq \mathbf{r}_0) \end{cases}. \quad (2.6)$$

where δ is the Dirac delta function. This initial condition signifies that the solution at time t depends solely on the particles that was initially at position $\mathbf{r}_0$ at $t = 0$.

In the case of free diffusion, where no geometrical limitations exist, the boundary condition is:

$$P(\mathbf{r}_0, \mathbf{r}_1 \to \infty, t) = 0, \quad (2.7)$$

Free diffusion yields a Gaussian propagator [3]**:**

$$P(\mathbf{r}_0, \mathbf{r}_1, t) = (4\pi Dt)^{-3/2} \exp\left[-(\mathbf{r}_1 - \mathbf{r}_0)^2/4Dt\right]. \quad (2.8)$$

In a homogenous system the propagator is independent of the initial position and depends only on the displacement $\mathbf{R} = \mathbf{r}_1 - \mathbf{r}_0$. This displacement corresponds to the probability $P(\mathbf{R},t)$:

$$P(\mathbf{R}, t) = (4\pi Dt)^{-3/2} \exp\left(-\mathbf{R}^2/4Dt\right). \quad (2.9)$$

In a heterogeneous system the propagator is no longer independent of starting position, an average propagator $P(\mathbf{R},t)$ is defined through

$$P(\mathbf{R}, t) = \int \rho(\mathbf{r}_0) P(\mathbf{r}_0, \mathbf{r}_0 + \mathbf{R}, t) d\mathbf{r}_0. \quad (2.10)$$

where the $\rho(\mathbf{r}_0)$ is the local density of the system. $P(\mathbf{r}_0, \mathbf{r}_0 + \mathbf{R}, t)$ gives the probability that a molecule has the displacement **R** during the time *t* averaged over all starting points $\mathbf{r}_0$.

Restricted diffusion occurs when molecules are constrained in their motion. Different geometrical constraints impose specific boundary conditions on diffusion equation and solving the diffusion equation yields corresponding solutions. In simple geometries, such as isolated pores with spherical, planar, or cylindrical shapes, analytical expressions for the propagator can be derived [19, 20], this will be further elaborated upon in Section 2.4.2. However, in more complex geometries, approximations or numerical methods are employed to estimate the propagator and solve the diffusion equation [21-23].

2.3 Exploring diffusion from microscopic molecular level

By examining the microscopic details of motion, we can gain insights into the overall macroscopic behaviour. The molecular level approach involves studying an ensemble of molecules, where we analyze the molecule's position or velocity as a function of time. When focusing on the molecule's position, the mean-square displacement is obtained by ensemble average of propagator and an apparent diffusion coefficient (ADC) depending on observation time. On the other hand, in the velocity approach, the evolution of a molecule's velocity is described using a velocity autocorrelation function and the diffusion spectrum.

2.3.1 Relationship between mean-square displacement and diffusion coefficient

The motion of a diffusing molecule is governed by a sequence of inter-molecule collisions, in this process, the position **r**(*t*) of individual molecule cannot be predicted with deterministic dynamics. Therefore, it is more convenient to describe the system based on its ensemble average properties. The fluctuations in the position **r**(*t*) can be measured using the mean-square displacement(MSD), which is defined as [3]**:**

$$\langle \mathbf{R}^2 \rangle = \langle (\mathbf{r}(t) - \mathbf{r}(0))^2 \rangle = \int_{-\infty}^{\infty} \mathbf{R}^2 P(\mathbf{R}, t) d\mathbf{R}. \qquad (2.11)$$

For free diffusion in a homogeneous medium, the probability density $P(\mathbf{R},t)$ is independent of the initial position and depends only on the displacement $\mathbf{R} = \mathbf{r}\text{-}\mathbf{r}_0$, as described in equation 2.9, the probability density is determined using a Gaussian

function. When equation 2.9 is substituted into equation 2.11, it produces the corresponding outcome for the mean square displacement:

$$\langle \mathbf{R}^2 \rangle = 2dDt. \qquad (2.12)$$

where d = 1,2,3 describes the dimensionality of the system. For the free diffusion, the D is truly a constant, identified as the free diffusion coefficient D_0.

When dealing with systems that have limitations, it is useful to establish an apparent diffusion coefficient (ADC) [3], denoted as

$$D(t) = \langle \mathbf{R}^2 \rangle / 2dt. \qquad (2.13)$$

The relationship between the ADC and diffusion time in restricted diffusion can be understood through Figure 2.3. This illustration shows the root-mean-squared displacement ($R_{\mathrm{rms}} = \sqrt{\langle \mathbf{R}^2 \rangle}$) of water molecules in both free and restricted diffusion scenarios. In free diffusion, R_{rms} of water molecules increases linearly with time, while in restricted diffusion within a pore of size $2a$, the R_{rms} reaches a plateau at approximately $2a$ for long diffusion durations. The presence of restrictions causes the ADC to deviate from the free diffusion coefficient of water when the observation period is long enough for molecules to encounter barriers. As the diffusion time increases, the ADC reflects the cumulative effect of restrictions experienced by diffusing molecules across various spatial scales [12].

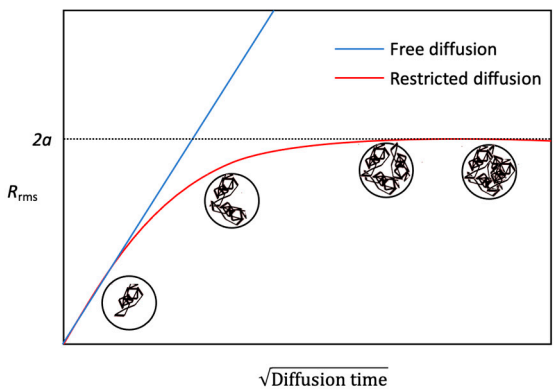

Figure2.3: Evolution of root-mean-squared displacement (R_{rms}) of water molecules over time: free vs.restricted diffusion. For free water, the R_{rms} increases linearly with time. However, for water molecules confined within a pore of characteristic dimension $2a$, the R_{rms} reaches a plateau at a value approximately equal to $2a$ for long diffusion times. The ADC (slope) remains constant over time in the asymptotic case and approaches zero when the boundaries are fully impermeable. Below this asymptotic limit, the ADC decreases with time, and the specific manner of decrease depends on the size and geometry of the pore. The figure is reproduced from ref. [12].

To be more specific, at the very short diffusion times, most molecules have not interacted with boundaries ($R_{rms} << 2a$) and diffusion is essentially free, $D(t)$ is close to the D_0. For sufficiently long times ($R_{rms} \approx 2a$), $D(t)$ levels off to an asymptotic value D_∞ reflecting the long-range connectivity of the porous network. During intermediate times, the molecules encounter the compartment boundary, but not all of them have had enough time to interact with the boundaries, resulting in a reduction in their R_{rms} compared to free diffusion. This decrease in diffusivity $D(t)$ strongly depends on the diffusion time and examining changes in $D(t)$ within the regime can provide valuable insights into the structural information of porous media. In the case of biological tissues, the relevant length scales correspond to the dimensions of cellular and sub-cellular structures, typically ranging in the order of a few micrometres. My thesis investigates the microscopic structure of biological tissues at precisely this scale.

2.3.2 Velocity autocorrelation and diffusion spectrum

Beginning with a simple one-dimensional situation where molecules move along the z-axis, the self-diffusion coefficients are also determined based on the velocity autocorrelation, and the Fourier transform of the velocity autocorrelations provides the frequency-dependent self-diffusion $D_\omega(\omega)$ [20]:

$$D_\omega(\omega) = \frac{1}{2}\int_{-\infty}^{\infty}\langle v(0)\cdot v(t)\rangle \exp(i\omega t)dt. \qquad (2.14)$$

here, $v(t)$ represents the instantaneous velocity of a molecule projected onto the z-axis. The velocity autocorrelation function $\langle v(0)\cdot v(t)\rangle$ quantifies how the velocity of molecules evolves over time. $\langle v(0)\cdot v(t)\rangle$ is commonly assumed to exponentially decay for the free diffusion:

$$\langle v(0)\cdot v(t)\rangle = \langle v^2\rangle \exp\left(\frac{-t}{\tau_v}\right). \qquad (2.15)$$

where $\langle v^2\rangle$ is the mean square velocity and τ_v represents the correlation time, indicating the time it takes for a molecule to "forget" its previous velocity. Substituting equation 2.15 into equation 2.14 yields:

$$D_\omega(\omega) = \frac{\langle v^2\rangle \tau_v}{1+\omega^2\tau_v^2}. \qquad (2.16)$$

If $\omega = 0$, equation 2.16 reduces to $D_\omega(0) = \langle v^2\rangle \tau_v = D_0$, which is the free diffusion coefficient.

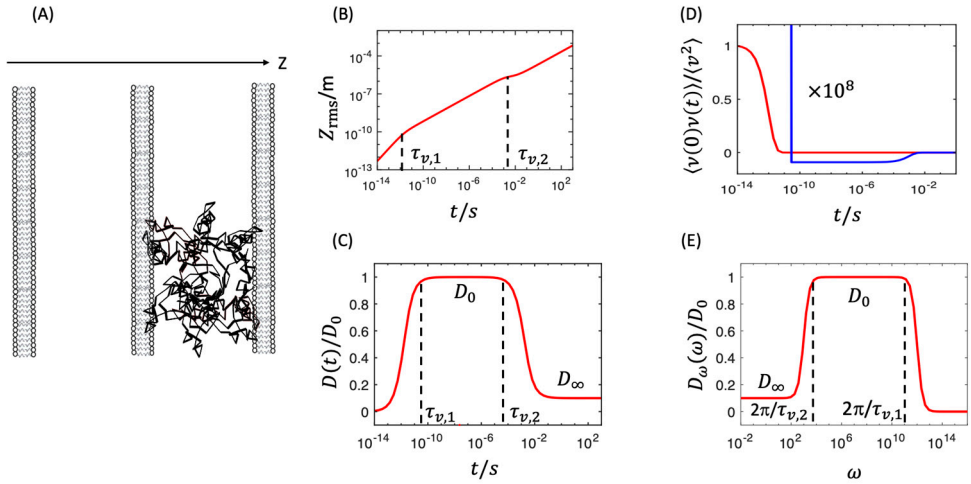

Figure 2.4: Comparative analysis of ADC for water in parallel permeable planes. (A) Porous System: water in an array of parallel permeable planes with a separation of 100 µm.(B) Root-mean-square displacement (Z_{rms}). (C) Apparent diffusion coefficient ($D(t)$). (D) Velocity autocorrelation function ($\langle v(0)v(t)\rangle$). The expansion highlights the long-time negative tail behavior of $\langle v(0)v(t)\rangle$.(E) Frequency-dependent diffusion coefficient ($D_\omega(\omega)$).

To summarize, the diffusion coefficient can be analysed over time using mean square displacement or in frequency using velocity autocorrelation. Figure 2.4 provides an example that compares the analysis of ADC for water within an array of parallel permeable planes with a separation of 100 µm using these two methods. For the sake of simplicity, we will focus on diffusion in the restricted dimension, denoted as "z". In this analysis, we assume that $\langle v(0)v(t)\rangle$ can be determined by [20]:

$$\langle v(0)v(\mathrm{t})\rangle = \frac{D_0}{\tau_{v,1}}\exp\left(-t/\tau_{v,1}\right) - \frac{(D_0-D_\infty)}{\tau_{v,2}}\exp\left(-t/\tau_{v,2}\right). \quad (2.17)$$

The first term, describing the time regime around the molecular correlation time [24], the second term describes the transition to the long-time behaviour [20].

Fourier transform of this equation yields:

$$D_\omega(\omega) = \frac{D_0}{1+\omega^2\tau_{v,1}^2} - \frac{D_0-D_\infty}{1+\omega^2\tau_{v,2}^2}. \quad (2.18)$$

and $\langle Z^2\rangle$ is given in equation [20]:

$$\langle Z^2\rangle = 2D_0\left\{t-\tau_{v,1}\left[1-\exp\left(-t/\tau_{v,1}\right)\right]\right\} - 2(D_0-D_\infty)\left\{t-\tau_{v,2}\left[1-\exp\left(-t/\tau_{v,2}\right)\right]\right\}. \quad (2.19)$$

and the $D(t)$:

$$D(t) = \frac{D_0}{t}\left\{t - \tau_{v,1}\left[1 - \exp\left(-\frac{t}{\tau_{v,1}}\right)\right]\right\} - 2(D_0 - D_\infty)\{t - \tau_{v,2}[1 - \exp(-t/\tau_{v,2})]\} \quad . \tag{2.20}$$

The value of $D(t)$ is acquired by substituting equation 2.19 into equation 2.13, where $d = 1$.

The functions mentioned above can be characterized by four parameters: the diffusion coefficient of the bulk liquid D_0, the long-time diffusion coefficient D_∞, the molecular correlation time $\tau_{v,1}$ and the wall-collision correlation time $\tau_{v,2}$. Figure 2.4 illustrates calculations for water using the following parameter values: $D_0 = 1.6\times10^{-9}\text{m}^2/\text{s}$, $D_\infty = D_0/10$, $\tau_{v,1} = 10^{-12}$ s and $\tau_{v,2} = 10^{-3}$ s. As expected, both $D(t)$ and $D_\omega(\omega)$ exhibit two plateau regions with values D_0 and D_∞. There are two transition regions between these plateaus: one occurs at $t = \tau_{v,1}$ and $\omega = 2\pi/\tau_{v,1}$, which is linked to molecular-level dynamics information; the other occurs at $t = \tau_{v,2}$ and $\omega = 2\pi/\tau_{v,2}$, which is associated with pore structure information. As shown in Figure 2.4 (D), the transition region from D_0 to D_∞, around time $\tau_{v,2}$, corresponds to a long-time negative tail of $\langle v(0)v(t)\rangle$. This observation implies a slightly higher probability for a molecule to change direction when diffusing within a pore. At this timescale (around $\tau_{v,2}$), studying diffusion process is sensitive to the macroscopic morphology of the pore system.

2.4 Anisotropic diffusion

Anisotropic diffusion is commonly observed in complex biological tissues and porous materials. Measurements of anisotropic diffusion provide valuable insights into the microstructural characteristics and orientations of these materials. In this context, we will introduce the relevant information on how to describe this process.

2.4.1 Anisotropic Gaussian diffusion

The diffusion of water within tissues is commonly characterized as an anisotropic process, often approximated through a second-order symmetric model [25-27]. Let's begin by introducing a straightforward scenario where the anisotropic process remains independent of time, known as Gaussian anisotropic diffusion. In the context of anisotropic Gaussian diffusion, the time-independent **D** can be depicted as a 3×3 matrix within Cartesian coordinates [26]:

$$\mathbf{D} = \begin{bmatrix} D_{xx} & D_{xy} & D_{xz} \\ D_{yx} & D_{yy} & D_{yz} \\ D_{zx} & D_{zy} & D_{zz} \end{bmatrix} = \mathbf{R}(\theta, \phi)\mathbf{D}^{\mathrm{PAS}}\mathbf{R}^{-1}(\theta, \phi), \quad (2.21)$$

where

$$\mathbf{D}^{\mathrm{PAS}} = \begin{bmatrix} D_{\perp} & 0 & 0 \\ 0 & D_{\perp} & 0 \\ 0 & 0 & D_{\parallel} \end{bmatrix}. \quad (2.22)$$

Here, θ and ϕ represent the polar and azimuthal angles, respectively, determining the orientation of the tensor in the laboratory frame, $\mathbf{R}(\theta, \phi)$ denotes the rotation matrix, and $D_{\parallel}$ and $D_{\perp}$ represent the eigenvalues parallel and perpendicular to the main symmetry axis of the compartment, respectively. Typically, for visualization purposes, the tensor $\mathbf{D}$ is parameterized with one quantity indicating size (D_{iso}), another indicating shape (D_{Δ}) and two parameters characterizing orientation (θ,ϕ) [26, 28], as depicted in Figure 2.5, where the diffusion patterns are rendered as superquadric tensor glyphs [29]. Expressions for D_{iso} and D_{Δ} can be given as:

$$D_{\mathrm{iso}} = \frac{D_{\parallel}+2D_{\perp}}{3}, \quad (2.23)$$

$$D_{\Delta} = \frac{1}{3D_{\mathrm{iso}}}(D_{\parallel} - D_{\perp}), \quad \in [-0.5,1]. \quad (2.24)$$

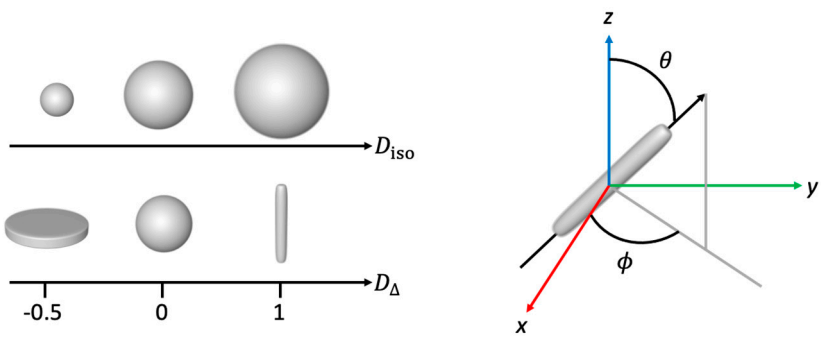

Figure 2.5: Quantitative measurements of diffusion tensor characteristics, including size (D_{iso}), shape (D_{Δ}), and orientation (θ, ϕ). The D_{iso} and D_{Δ} parameters provide information about the magnitude and anisotropy of the underlying diffusion process. The polar angle θ and azimuthal angle ϕ define the orientation of the diffusion tensor in relation to the laboratory frame of reference.

The (D_{iso}, D_{Δ}, θ, ϕ) parameter set offers a comprehensive description of an axisymmetric Gaussian anisotropic diffusion tensor, with each parameter capturing

a distinct aspect of the tensor's geometry. This connection between the microenvironment's structure and the localized diffusion pattern is exemplified in Figure 2.6. Each microscopic **D** is closely tied to the geometry of the surrounding medium and can be interpreted as a diffused representation of the local structure.

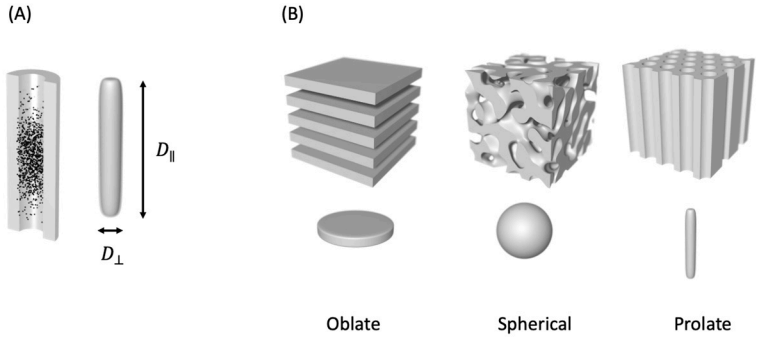

Figure 2.6: Schematic representation highlighting the connection between pore space geometries and diffusion tensors. (A) Demonstrates diffusion within a cylinder along with the corresponding prolate diffusion tensor, $D_{\parallel}$ and $D_{\perp}$ indicate eigenvalues aligned parallel and perpendicular, respectively. (B) Presents the shapes of pore space geometries (top row, left to right: Plane, Sphere and Cylinder) alongside the respective shapes of the diffusion tensors (bottom row, left to right: Oblate, Spherical, Prolate).

2.4.2 Anisotropic-restricted diffusion

In general, the diffusion process is anisotropic and restricted, then the isotropic diffusion coefficient D in equation 2.1 is replaced by a second order symmetric diffusion tensor **D** [27], the equation 2.1 becomes [3]:

$$\begin{bmatrix} J(x,t) \\ J(y,t) \\ J(z,t) \end{bmatrix} = - \begin{bmatrix} D_{xx} & D_{xy} & D_{xz} \\ D_{yx} & D_{yy} & D_{yz} \\ D_{zx} & D_{zy} & D_{zz} \end{bmatrix} \begin{bmatrix} \frac{\partial c(x,t)}{\partial t} \\ \frac{\partial c(y,t)}{\partial t} \\ \frac{\partial c(z,t)}{\partial t} \end{bmatrix}, \tag{2.25}$$

The corresponding equation 2.3 becomes:

$$\frac{\partial c(\mathbf{r},t)}{\partial t} = \nabla \cdot \mathbf{D} \cdot \nabla c(\mathbf{r},t). \tag{2.26}$$

In the case of anisotropic restricted diffusion, the equation 2.5 becomes:

$$\frac{\partial P(\mathbf{r}_0,\mathbf{r}_1,t)}{\partial t} = \nabla \cdot \mathbf{D} \cdot \nabla P(\mathbf{r}_0,\mathbf{r}_1,t). \tag{2.27}$$

D is a time-dependent diffusion tensor. It can also be represented as a function of frequency, known as the diffusion spectrum **D**(ω) [3, 12].

In the principal axis system (PAS), all off-diagonal elements are 0, three eigenvalues are the diagonal elements. In this case, **D**(ω) can be written as

$$\mathbf{D}(\omega) = \begin{bmatrix} D_{\mathbf{11}}(\omega) & 0 & 0 \\ 0 & D_{\mathbf{22}}(\omega) & 0 \\ 0 & 0 & D_{\mathbf{33}}(\omega) \end{bmatrix}. \quad (2.28)$$

For an axisymmetric tensor, using the example of diffusion restricted within a cylinder, the eigenvalues perpendicular to the cylinder axis are given by $D_{\text{rest}}(\omega) = D_{11}(\omega) = D_{22}(\omega)$, while the eigenvalue parallel to the cylinder axis is D_0. **D**(ω) can be expressed as:

$$\mathbf{D}(\omega) = \begin{bmatrix} D_{\text{rest}}(\omega) & 0 & 0 \\ 0 & D_{\text{rest}}(\omega) & 0 \\ 0 & 0 & D_0 \end{bmatrix}. \quad (2.29)$$

For the diffusion restricted within a planar case, the **D**(ω) is obtained by exchanging $D_{\text{rest}}(\omega)$ and D_0.

For a liquid with a bulk diffusivity D_0 confined in d dimensions in planar (d = 1), cylindrical (d = 2), or spherical (d = 3) compartments with a radius of a, the diffusion spectrum **D**(ω) in the restricted dimensions can be expressed as follows [20]:

$$D_{\text{rest}}(\omega) = D_0 - \sum_k \omega_k \frac{D_0 - D_\infty}{1 + \omega^2/\Gamma_k^2}. \quad (2.30)$$

where

$$\Gamma_k = \frac{\xi_k^2 D_0}{a^2} \quad (2.31)$$

and

$$\omega_k = \frac{2}{\xi_k^2 + 1 - d}. \quad (2.32)$$

In equation 2.31 and 2.32, ξ_k is the kth solution of

$$\xi J_{d/2-1}(\xi) - (d-1) J_{d/2}(\xi) = 0. \quad (2.33)$$

where J_n is the nth-order Bessel function of the first kind.

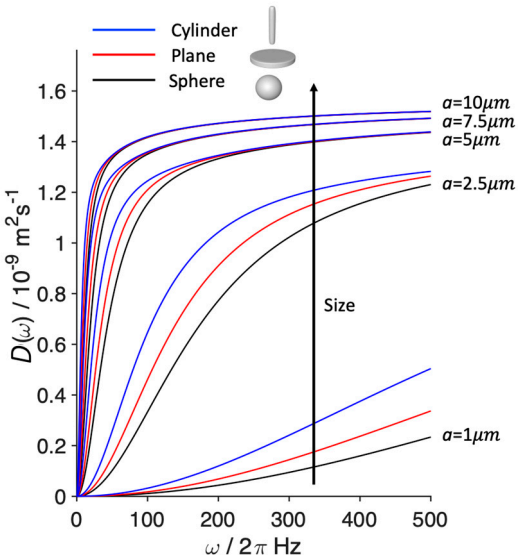

Figure 2.7: Relationship between ADC ($D_{rest}(\omega)$) and oscillation frequency for various sizes and geometries of impermeable compartments. The frequency range extends up to 500 Hz, covering different compartments: spheres, planes, and cylinders, each characterized by a radius (a) ranging from 1 μm to 10 μm. The curves of different colors correspond to different shapes of compartments: spheres (black), planes (red), and cylinders (blue).

Figure 2.7 illustrates the dependence of ADC dispersion ($D_{rest}(\omega)$) on the oscillation frequency range for various sizes and geometries of impermeable compartments, the calculations are based on expressions demonstrated in equations 2.30-2.33. The frequency range spans up to 500 Hz and encompasses diverse compartments: spheres, planes, and cylinders, each characterized by a radius (a) ranging from 1 μm to 10 μm. The curves of different colors represent distinct compartment shapes: spheres (black), planes (red), and cylinders (blue). As depicted in the figure, ADC ($D_{rest}(\omega)$) is closely linked to the sizes and shapes of the compartments. Utilizing the variation of ADC with oscillation frequency has been a technique utilized for estimating the dimensions of restricting structures within porous media, encompassing scenarios like densely packed cells and microcapillaries [30-32]. This method relies on the fitting of NMR measurements at varying frequencies to analytical models of restricted diffusion within uncomplicated geometries, such as impermeable planes, cylinders, or spheres [20, 33].

The symmetric second-order diffusion tensor $\mathbf{D}(\omega)$ in the equation 2.29 can be represented as a 3×3 matrix in Cartesian coordinates:

$$\mathbf{D_{rest}}\,(\omega) = \begin{bmatrix} D_{xx} & D_{xy} & D_{xz} \\ D_{yx} & D_{yy} & D_{yz} \\ D_{zx} & D_{zy} & D_{zz} \end{bmatrix} =$$

$$\mathbf{R}(\theta,\phi)\begin{pmatrix} D_{\mathrm{rest}}(\omega) & 0 & 0 \\ 0 & D_{\mathrm{rest}}(\omega) & 0 \\ 0 & 0 & D_0 \end{pmatrix}\mathbf{R^{-1}}(\theta,\phi) \qquad (2.34)$$

where θ and φ are polar and azimuthal angles, giving the orientation of the cylinder in the lab frame, and $\mathbf{R}(\theta, \varphi)$ is the rotation matrix.

At higher values of ω, $D_{\mathrm{rest}}(\omega)$ approaches D_0, indicating isotropic diffusion. On the other hand, the effects of anisotropy become more prominent in the low-ω limit, where $D_{\mathrm{rest}}(\omega)$ approaches D_∞, that means it is ω-independent, which is described in the 2.4.1, anisotropic Gaussian diffusion.

3 NMR

Nuclear Magnetic Resonance (NMR) is a powerful technique used for probing the molecular and atomic properties of materials. It is based on the principle that certain atomic nuclei possess intrinsic magnetic properties and can resonate when placed in a magnetic field and exposed to radiofrequency (RF) radiation [34]. NMR provides valuable insights into the structure, dynamics, and interactions of molecules in various environments [35-37], including liquids, solids, and gases. In addition to its applications in chemistry and physics, NMR has found extensive use in fields like medicine, where it is employed in Magnetic Resonance Imaging (MRI) to visualize internal structures of the human body [38, 39].

While the focus of this thesis centres on introducing an innovative MRI technique, the NMR section provides crucial NMR insights specifically tailored for the MRI framework. Importantly, the semi-classical vector model plays a central position in the MRI domain, simplifying the intricacies of NMR through classical physics principles. This model visualizes the magnetic moments of atomic nuclei as vectors, providing an intuitive understanding of their precession and relaxation behaviour within external magnetic fields.

The NMR section begins with the basics of NMR, followed by discussions on diffusion NMR (including encoding motion, pulse sequence), and diffusion tensor imaging.

3.1 Basics of NMR

The section discusses the essential principles, including the magnetization vector, Larmor precession, RF-pulse, and relaxation mechanisms (inversion, recovery). This section is based on the textbook of Keeler [34].

3.1.1 Magnetization vector

A nucleus with a nonzero spin generates a small magnetic field that behaves similarly to a miniature bar magnet. This physical quantity is named the spin magnetic moment. Within a sample, there are thousands of these tiny bar magnets randomly distributed. When the sample is exposed to a magnetic field for a

sufficient duration, it becomes magnetized, resulting in a net magnetic moment for the entire sample. This net magnetic moment is known as bulk magnetization($\mathbf{M}_0$), which can be represented as a vector aligned with the direction of the applied magnetic field. The process by which the net bulk magnetization reaches its equilibrium value is depicted in Figure 3.1.

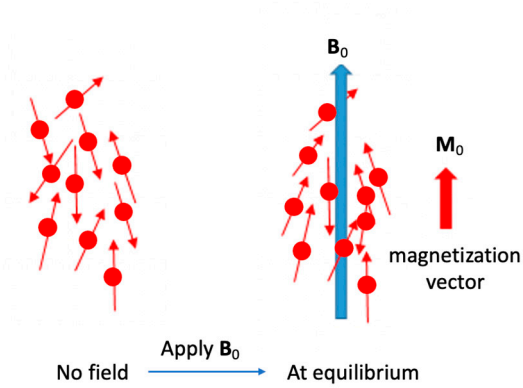

Figure 3.1 The process of forming magnetiztion vector ($\mathbf{M}_0$). In the absence of a magnetic field (left panel), the bar magnets are randomly oriented, resulting in no overall magnetization. When a magnetic field is applied($\mathbf{B}_0$) and given enough time, the bar magnets align more towards the field direction (right panel), leading to a net magnetization along the field direction.

3.1.2 Larmor precession

Larmor precession is a fundamental phenomenon in the field of NMR, it refers to the tilted magnetization vector moving away from the z-axis and precessing along the direction of the applied magnetic field, sweeping out a cone of constant angle relative to the *z*-axis. This motion, known as Larmor precession, occurs at a frequency denoted as $\omega_0 = -\gamma B_0$, where γ represents the gyromagnetic ratio and B_0 is the strength of the applied magnetic field. By placing a small coil of wire in the *xy*-plane, the precession of the tilted magnetization vector cuts through the coil, inducing an electric current and recording a signal known as free induction decay (FID). Figure 3.2 illustrates the precession of the tilted magnetization vector rotating about the direction of the applied magnetic field, resulting in the generation of a signal.

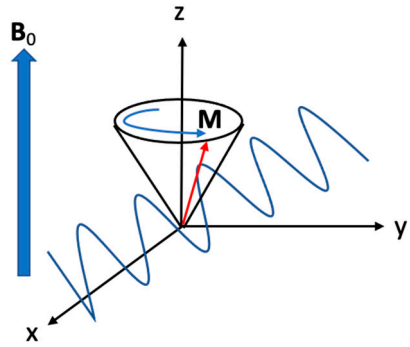

Figure3.2 The precession motion of the tilted magnetization vector (**M**) rotating around the direction of the applied magnetic field. The precessing magnetization cuts a coil positioned around the *x*-axis, resulting in the induction of an electric current.

3.1.3 RF-pulse

As discussed above, the Larmor precession of the tilted magnetization vector can be detected. The question arises: How can we deviate the magnetization vector from its equilibrium position? In NMR, one of its strengths lies in the ability to manipulate these magnetization vectors with great flexibility. A common approach to deviate the magnetization vector from its equilibrium position along the *z*-axis, involving the rapid application of a magnetic field along the *x*-axis, denoted as $\mathbf{B}_1$, this technique enables the generation of the required oscillating magnetic field by applying radiofrequency (RF) power to the coil, thereby creating the RF field along the *x*-direction. This causes the bulk magnetization **M**, to precess around the *x*-axis, resulting in the magnetization tilting towards the transverse plane. These physical quantities satisfy the Bloch equation [40]:

$$\frac{d\mathbf{M}}{dt} = \mathbf{M} \times \gamma \mathbf{B}_1 \qquad (3.1)$$

The equation provides a semi-classical representation of NMR and is highly valuable in our study. The precession frequency is determined as $\omega_1 = -\gamma B_1$. When the pulse is precisely synchronized with the Larmor precession (on-resonance), the equilibrium magnetization vector undergoes a simple rotation in the *yz*-plane starting from the *z*-axis, as illustrated in Figure 3.3. The flip angle of the pulse, denoted as β, is determined by $\beta = \omega_1 t_p$, where ω_1 represents the precession frequency and t_p represents the duration of the RF pulse application. Commonly used flip angles are 90° or 180°, which calls a 90° or 180° pulse.

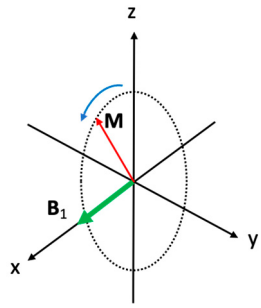

Figure 3.3: The precession of the magnetization vector (**M**) around the *x*-axis when a pulse is applied along the *x*-axis. This precession direction of **M** adheres to the right-hand rule: if we extend our right hand so that the thumb and other fingers are mutually perpendicular, the thumb points to the direction of the applied the pulse ($\mathbf{B}_1$), and the alignment of the four fingers indicates the initial direction of **M**. The curling direction of the four fingers signifies the rotation direction of **M**.

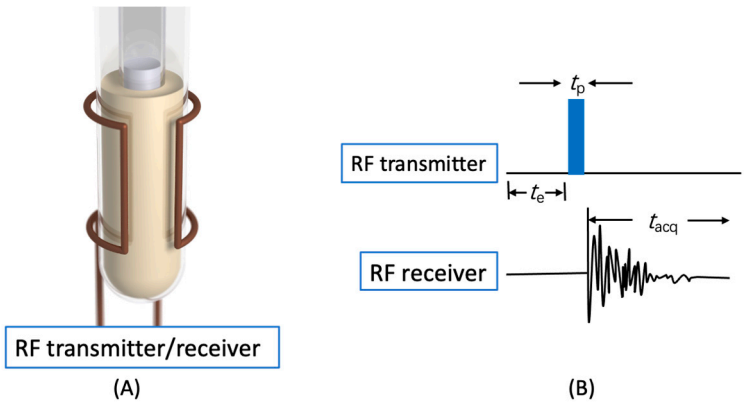

Figure 3.4: The basic pulse-acquire experiment. (A) Illustration of a typical spectroscopic NMR setup, employing saddle-shaped RF coils for both transmitter and receiver. Adapted with permission for ref. [41] (B) This diagram demonstrates the procedure for recording a basic NMR spectrum, where t_p represents the pulse duration, t_e is the time during which equilibrium magnetization **M** builds up, and t_{acq} is the acquisition time for the FID spectrum.

Then, we demonstrate the acquisition of a simple FID through pulse experiments. Figure 3.4 illustrates the experimental setup and corresponding pulse sequence for a basic pulse-acquire experiment. In Figure 3.4(A), the sample volume, enclosed by the RF transmitter coil, is irradiated with an RF-pulse, which excites the spins. The resulting signal is received by an RF receiver. As depicted in Figure 3.4(B), t_e represents the time during which equilibrium magnetization **M** builds up, and t_p denotes the duration of the pulse, which is typically very short. Subsequently, t_{acq} time is needed to acquire the FID spectrum. By performing Fourier transform, the frequency-domain spectrum can be obtained. Since NMR signals are usually weak due to the small gyromagnetic ratio, conducting multiple measurements and summing their FID profiles improves the signal-to-noise ratio.

3.2 Relaxation

Immediately following the 90° pulse, the strength of magnetization was flipped in the *xy*-plane. However, the magnetization in the *xy*-plane starts to decay, this decay occurs through two distinct processes [42]. The first process is known as T_1 relaxation or longitudinal relaxation, where the spin ensemble returns to thermal equilibrium. The second process is referred to as T_2 relaxation or transverse relaxation, also known as spin-spin relaxation. T_2 relaxation is caused by dipolar interactions between spins. The spins can experience fluctuating magnetic fields due to neighbouring spins, resulting in a phase shift caused by changing precession frequencies.

The Bloch equations 3.1 can be modified to include the effects of relaxation [43]:

$$\begin{aligned}
\frac{\partial M_x}{\partial t}(\mathbf{r},t) &= \gamma(\mathbf{M}\times\mathbf{B_1})_x - \frac{M_x(\mathbf{r},t)}{T_2}.\\
\frac{\partial M_y}{\partial t}(\mathbf{r},t) &= \gamma(\mathbf{M}\times\mathbf{B_1})_y - \frac{M_y(\mathbf{r},t)}{T_2}.\\
\frac{\partial M_z}{\partial t}(\mathbf{r},t) &= \gamma(\mathbf{M}\times\mathbf{B_1})_z - \frac{(M_z(\mathbf{r},t)-M_0(\mathbf{r}))}{T_1}.
\end{aligned} \tag{3.2}$$

and the corresponding solutions as below:

$$\begin{aligned}
M_x(t) &= M_0 \sin(\omega_0 t)\exp(-t/T_2).\\
M_y(t) &= M_0 \cos(\omega_0 t)\exp(-t/T_2).\\
M_z(t) &= M_0 [1 - \exp(-t/T_1)].
\end{aligned} \tag{3.3}$$

The following sections will discuss how to measure T_1 and T_2 relaxation time in NMR.

3.2.1 Inversion recovery

The conventional approach to measure T_1 relaxation is through the utilization of inversion recovery. Figure 3.5 illustrates the pulse sequence [4] employed in this method. Initially, the magnetization is inverted from the equilibrium +*z* direction to the -*z* axis using a 180° pulse. Over time, the magnetization gradually relaxes back towards equilibrium during the signal evolution. Following a time delay, τ, a 90° pulse is applied to flip the magnetization to the *xy*-plane, and the resulting signal is detected. The amplitude of the magnetization in the *xy*-plane can be described by the equation:

$$M(\tau) = M_0 [1 - 2\exp(-\tau/T_1)]. \quad (3.4)$$

By conducting the experiment with different values of τ and fitting the acquired data to equation 3.4, the T_1 relaxation time can be determined.

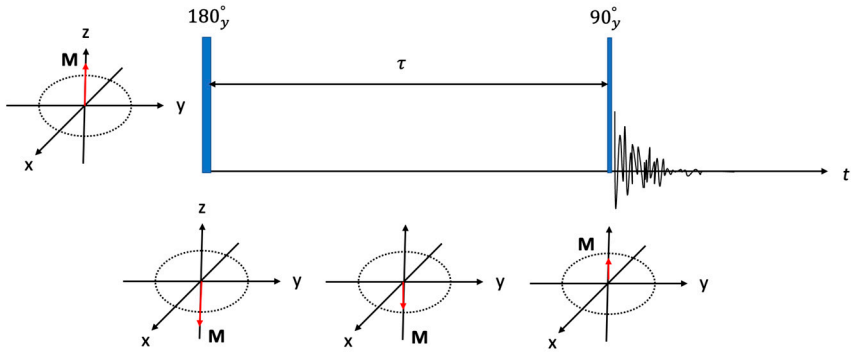

Figure 3.5: Pulse sequence of inversion recovery and its impact on the magnetization vector. The initial magnetization before the RF-pulse is represented by red arrows, by applying a 180° pulse, the magnetization undergoes a rotation around the y-axis and becomes inverted. During the evolution time τ, the magnetization gradually relaxes towards equilibrium through T_1 relaxation. The 90° pulse then flips the magnetization back to the *xy*-plane, enabling its detection.

3.2.2 Spin-echo

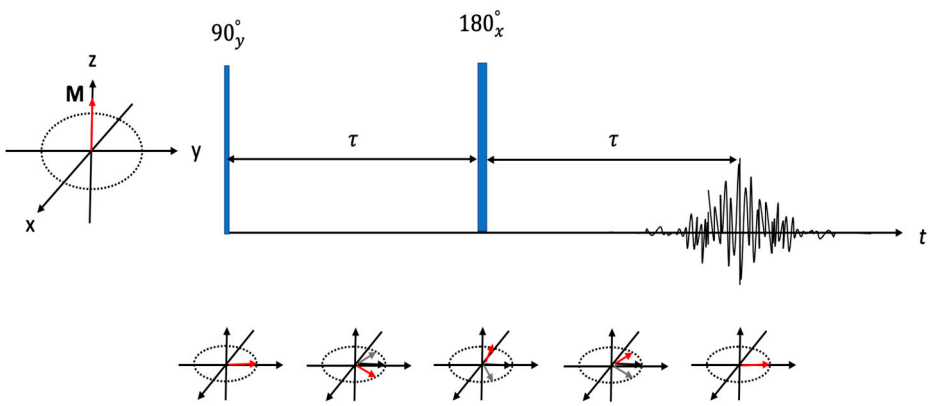

Figure 3.6: Spin-echo (SE) pulse sequence and its impact on the magnetization vector. Initially, before the first RF pulse, the magnetization is in equilibrium and directed along the *z*-axis. The 90° pulse rotates the magnetization around the *y*-axis, placing it in the xy-plane with an orientation along the *x*-axis. During the first evolution time, τ , the magnetization is subjected to transverse relaxation. The 180° pulse then inverts the magnetization by rotating it around the *x*-axis. During the second evolution time, the dephasing caused by spatial field inhomogeneities is subsequently rephased, resulting in the generation of an echo after a total delay of 2τ.

T_2 relaxation can be effectively measured using the spin-echo technique [44], as demonstrated in Figure 3.6. The process commences with a 90° pulse, causing the magnetization to reside in the *xy*-plane where it evolves over time. Subsequently, a 180° pulse is applied to invert the magnetization after a delay of τ. During the second delay, the signal continues to evolve with the opposite direction of the first delay. Upon a total delay of 2τ, the dephasing resulting from spatial field inhomogeneities relaxation is refocused, leading to the formation of an echo. However, the transverse relaxation caused by conventional T_2 relaxation remains unrefocused, causing a reduction in magnetization as described by the equation:

$$M(2\tau) = M_0 \exp(-2\tau/T_2). \quad (3.5)$$

To determine the value of T_2, the experiment is repeated using different τ values, and T_2 is obtained by fitting equation 3.5 to the corresponding experimental data.

The spin-echo pulse sequence serves as a fundamental NMR experiment, commonly incorporated into more complex studies, such as this method offers notable advantages in diffusion and imaging sequences by successfully refocusing the magnetization lost due to spatial field inhomogeneities [5], which will be detailed in the following section.

3.3 Diffusion NMR

In this section, we will present the fundamental principles of diffusion NMR, including how magnetic field gradients are utilized to encode translational motion and implement pulsed gradient spin echo sequence. Additionally, we will introduce diffusion tensor imaging.

3.3.1 Encoding of translational motion by magnetic field gradients

In diffusion NMR experiments, magnetic field gradients are used to sensitize the transverse magnetization to the diffusive motion of molecules [45]. The diffusion NMR signal is given by an ensemble average of a large number of spin contributions:

$$s(t) = s_0\langle \exp\,[i\phi(\mathbf{r},t)]\rangle = s_0 \int P(\phi,t)\exp[i\phi(\mathbf{r},t)]d\phi. \quad (3.6)$$

where s_0 represents the relaxation weighted signal magnitude, the ensemble average term $\langle\cdots\rangle$ is generally complex and can introduce a non-zero signal phase. However, its magnitude is always smaller than unity, leading to signal attenuation. The $\phi(\mathbf{r}, t)$ is the time-dependent phase of a single spin with gyromagnetic ratio γ,

$$\phi(\mathbf{r},t) = -\gamma \int_0^t \mathbf{g}(t') \cdot \mathbf{r}(t') d\, t'. \qquad (3.7)$$

where $\mathbf{g}(t')$ is the time-dependent magnetic field gradient, which is often referred to as the gradient waveform. $\mathbf{r}(t')$ is the spin trajectory. The interplay between $\mathbf{g}(t')$ and $\mathbf{r}(t')$ results in $\phi(\mathbf{r},t)$ evolving from zero at $t = 0$ to periodic patterns with varying directions and spatial wavelengths at intermediate times.

The effect of the gradient on the phase of the spins is quantified by the dephasing q-vector, which is given by:

$$\mathbf{q}(t) = \gamma \int_0^t \mathbf{g}(t') dt'. \qquad (3.8)$$

3.3.2 Pulsed gradient spin-echo

The most commonly used method for estimating diffusion parameters is the pulsed gradient spin echo (PGSE) experiment, which was introduced by Stejskal and Tanner in 1965 [5]. The details of this method are explained below.

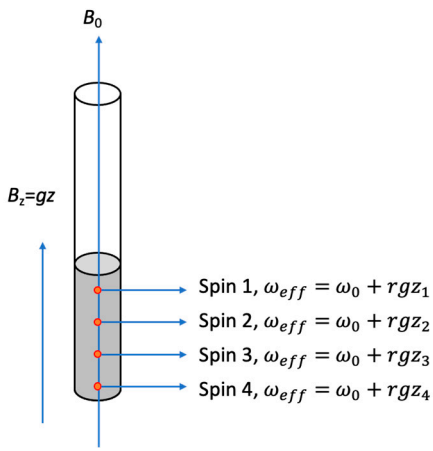

Figure 3.7: Spin frequency variation in linearly inhomogeneous field. The spin frequency (ω_{eff}) in an inhomogeneous field that exhibits a linear variation across the sample volume in Z direction , with z_1, z_2, z_3 and z_4 denoting distinct positions of spins within the sample. The total magnetic field is the combination of the homogeneous main magnetic field (B_0)and the applied field gradient (B_Z).

Pulsed gradient is that a magnetic field gradient with a constant gradient strength is applied along the z-axis, as shown in Figure 3.7, the resulting magnetic field along the z-axis is given by:

$$B_0^{'} = B_0 + gz. \qquad (3.9)$$

The precession frequency of the spins is determined by:

$$\omega_{eff}(z) = \gamma B_0^{'} = \gamma B_0 + \gamma g z = \omega_0 + \gamma g z. \qquad (3.10)$$

The precession frequency of the spins depends on their position, allowing us to label the spins in different positions. Depending on whether the field gradient strength is higher or lower than B_0, the spins will precess faster or slower than ω_0. During the application of the magnetic field gradient, the spin acquires a phase difference, ϕ, which depends on its position, $\mathbf{r}$, the gradient duration, $t = \delta$, and the gradient strength, g, according to:

$$\phi(\mathbf{r}, t) = -\gamma \int_0^t \mathbf{g}(t') \cdot \mathbf{r}(t') d\, t' = -\gamma \delta \mathbf{g} \cdot \mathbf{r}, \qquad (3.11)$$

the corresponding dephasing q-vector in the equation 3.8, which is given by:

$$\mathbf{q}(t) = \gamma \int_0^t \mathbf{g}(t') dt' = \gamma \delta\, \mathbf{g}. \qquad (3.12)$$

Figure 3.8 presents a schematic diagram of the pulse sequence. A field gradient of length δ and strength g is applied between the two RF pulses and after the 180º pulse. During the gradient application, the Larmor frequency is spatially encoded, resulting in distinct precession rates for molecules at different locations. The 180º pulse flips the magnetization signal along the z-axis, making the two gradient blocks effectively opposite in sign. Consequently, if the molecule remains stationary, the dephasing caused by the initial gradient is reversed by the second gradient. However, if the spins move along the **z**-axis during the duration Δ, the effects of the first gradient are not counteracted by the second, leading to dephasing, $\Delta\phi(\mathbf{r}) = \mathbf{q} \cdot (\mathbf{r} - \mathbf{r}_0)$. This dephasing causes a decay in the intensity of the signal.

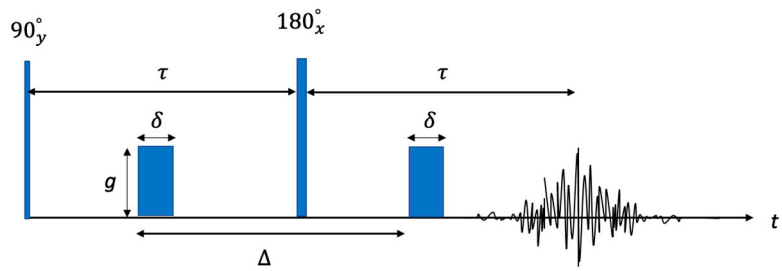

Figure 3.8: The pulse gradient spin echo (PGSE) sequence. The echo is observed at 2τ. Positioned between the two RF pulses (90º pulse and following 180º pulse), there are two pulse magnetic field gradients with a duration of δ and a strength of g.

For simplicity in the case of free diffusion, we provide a brief classical derivation of the signal attenuation in PGSE NMR diffusion experiments to theoretically

describe the effect of translational diffusion on the spin echo. This derivation will be presented in terms of the macroscopic transverse magnetization $M_{xy}(\mathbf{r},t)$, combining the Bloch equation with Fick's second law gives [3, 43, 46]:

$$\frac{\partial M_{x,y}}{\partial t} = -\frac{M_{x,y}}{T_2} - i\gamma[\mathbf{g}(t)\cdot\mathbf{r}]M_{x,y} + D\nabla^2 M_{x,y}. \tag{3.13}$$

the solution of the equation is:

$$\begin{aligned} M_{x,y}(t) &= M_0 \exp\left(-\frac{t}{T_2}\right)\cdot\langle\exp[i\phi(\mathbf{r},t)]\rangle \\ &= M_0 \exp\left(-\frac{t}{T_2}\right)\exp\left(-i\gamma\mathbf{q}(t)\cdot\mathbf{r} - D\int_0^t \mathbf{q}(t')\cdot\mathbf{q}(t')\,dt'\right) \end{aligned} \tag{3.14}$$

at the echo time 2τ, the echo condition $\mathbf{q}(2\tau) = 0$ is fulfilled, insert equation 3.12 into equation 3.14, we obtain:

$$\begin{aligned} M_{x,y}(2\tau) &= M_0 \exp\left(-\frac{2\tau}{T_2}\right) M_{x,y}(\mathrm{g},\Delta) \\ &= M_0 \exp\left(-\frac{2\tau}{T_2}\right)\exp\left(-(\gamma \mathrm{g}\delta)^2\left(\Delta - \frac{\delta}{3}\right)\cdot D\right) \end{aligned} \tag{3.15}$$

Next, let $S(t)$ and $S(0)$ denote the signal intensity at time t with and without magnetic field gradients, respectively. The signal $S(0)$ solely accounts for the relaxation effect. Thus, the equation can be expressed as:

$$S(b) = S(0)\exp(-bD). \tag{3.16}$$

where

$$b = (\gamma \mathrm{g}\delta)^2(\Delta - \tfrac{\delta}{3}). \tag{3.17}$$

In these equations, D represents the diffusion coefficient, $S(0)$ is the signal amplitude in the absence of diffusion, and the quantity b reflects the encoding is determined by the specific encoding pulse sequences used. For the PGSE sequence, $b = (\gamma g\delta)^2(\Delta - \delta/3)$. By adjusting the parameter b through encoding pulses and fitting the measured $S(b)$ according to equation 3.16, the diffusion coefficient D can be estimated. It should be noted that equation 3.16 is only valid when there is a single isotropic diffusing component.

3.4 Diffusion tensor imaging

For the case of anisotropic diffusion, and the equation 3.13 is rewritten as follows with diffusion tensor[3, 4]:

$$\frac{\partial M_{x,y}(\mathbf{r},t)}{\partial t} = -\frac{M_{x,y}}{T_2} - [-i\gamma \mathbf{g}(t)\cdot\mathbf{r}]M_{x,y}(\mathbf{r},t) + \nabla\cdot\mathbf{D}\cdot\nabla M_{x,y}(\mathbf{r},t). \tag{3.18}$$

where $\mathbf{g}(t)$ is the effective diffusion gradient waveform. This equation has the solution:

$$M_{x,y}(\mathbf{r},t) = M_0 \exp\left(-\frac{2\tau}{T_2}\right) \exp\left(-i\mathbf{q}(t)\cdot\mathbf{r} - \int_0^t \mathbf{q}^{\mathrm{T}}(t')\cdot\mathbf{D}\cdot\mathbf{q}(t')dt'\right) \tag{3.19}$$

where M_0 is the initial magnetization at time $t = 0$.

Here, for the spin-dephasing vector q-vector in the equation 3.8, we introduce a new representation with a $q(t)$ denotes the time-dependent norm and $\mathbf{n}(t)$ signifies the unit orientation, as illustrated below:

$$\mathbf{q}(t) = \gamma \int_0^t \mathbf{g}(t')dt' = q(t)\mathbf{n}(t). \tag{3.20}$$

Typically, diffusion NMR measurements acquire the signal at time 2τ, where the echo condition $\mathbf{q}(2\tau) = 0$ is fulfilled, nullifying the imaginary term in the equation 3.19.

The magnetization is measured across an MRI voxel, typically a volume on the millimetre-scale. The overall signal "S" is the integral over the volume "V" of $M_{x,y}(\mathbf{r},t)\mathrm{d}\mathbf{r}$, representing an average of contributions from various microscopic environments, each potentially exhibiting distinct diffusion behaviour. Assuming that the distinct diffusion microscopic environments within the sample are non-exchanging, the macroscopic signal can be expressed by integrating $M_{x,y}(\mathbf{r},t)$ over the examined sample volume to obtain the signal "S" as described by [47]:

$$S = S_0 \int P(\mathbf{D})\exp\left(-\int_0^\tau q^2(t)\mathbf{n}^{\mathrm{T}}(t)\cdot\mathbf{D}\cdot\mathbf{n}(t)\mathrm{d}t\right)\mathrm{d}\mathbf{D} \tag{3.21}$$

Similar to equation 3.16, S and S_0 represent the signal intensity at time t with and without magnetic field gradients, respectively. $P(\mathbf{D})$ is a continuous diffusion tensor distribution.

Then, introducing the encoding tensor (or **b**-tensor) [3, 4]:

$$\mathbf{b} = \int_0^\tau q^2(t)\mathbf{n}(t) \cdot \mathbf{n}^{\mathrm{T}}(t)dt. \quad (3.22)$$

The **b**-tensor can also be expressed as the tensor-valued encoding spectrum $\mathbf{b}(\omega)$, which varies with frequency. The spectrum of the encoding tensor $\mathbf{b}(\omega)$ is derived from time-dependent gradient vector $\mathbf{g}(t)$, time-dependent dephasing vector $\mathbf{q}(t)$, and spectrum of the dephasing vector $\mathbf{q}(\omega)$ [12, 45],

$$\mathbf{q}(\omega) = \int_0^\tau \mathbf{q}(t) \exp(\mathrm{i}\omega t)\, \mathrm{d}t, \quad (3.23)$$

$$\mathbf{b}(\omega) = \frac{1}{2\pi}\mathbf{q}(\omega)^{\mathrm{T}} \cdot \mathbf{q}(-\omega). \quad (3.24)$$

The equation 3.21 rewrite as:

$$\frac{S[\mathbf{b}(\omega)]}{S_0} = \int P[\mathbf{D}(\omega)]\exp\Big(-\int_{-\infty}^{\infty} \mathbf{b}(\omega) : \mathbf{D}(\omega)\mathrm{d}\omega\Big)\mathrm{d}\mathbf{D}(\omega) \quad (3.25)$$

where, $P[\mathbf{D}(\omega)]$ is the continuous diffusion spectrum distributions, also denote $\mathbf{D}(\omega)$-distribution, and

$$\mathbf{b}(\omega) : \mathbf{D}(\omega) = \sum_i \sum_j b_{ij}(\omega) D_{ij}(\omega) \quad (3.26)$$

When the complete ω-dependent and tensorial representation of $\mathbf{b}(\omega)$ is utilized for encoding experimental data, it is helpful to summarize its key aspects using centroid frequency ω_{cent} [48], the magnitude b [49, 50] and the normalized anisotropy b_Δ [51]. These variables are defined through the following equations:

$$b(\omega) = \mathrm{trace}\{\mathbf{b}(\omega)\}. \quad (3.27)$$

$$\omega_{\mathrm{cent}} = \frac{\int_{-\infty}^{\infty} |\omega| b(\omega)\mathrm{d}\omega}{\int_{-\infty}^{\infty} b(\omega)\mathrm{d}\omega}. \quad (3.28)$$

$$\mathbf{b} = \int_{-\infty}^{\infty} \mathbf{b}(\omega)\mathrm{d}\omega. \quad (3.29)$$

$$b = \mathrm{trace}\{\mathbf{b}\} = \int_{-\infty}^{\infty} b(\omega)\mathrm{d}\omega \quad (3.30)$$

and

$$b_\Delta = \frac{1}{b}\left(b_{\mathrm{zz}} - \frac{b_{\mathrm{yy}} + b_{\mathrm{xx}}}{2}\right). \quad (3.31)$$

In equation 3.29, **b** is the conventional (ω -independent) b-matrix [49], b_{xx}, b_{yy} and b_{zz} are the eigenvalues [52].

In summary, the sensitivity of the MRI signal to different types of motion can be measured using the tensor-valued encoding spectrum $\mathbf{b}(\omega)$ [45, 53]. The trace of this spectrum represents the dephasing power spectrum [20], which is relevant for isotropic restricted diffusion. The integral of the spectrum over ω corresponds to the conventional b-matrix [49], providing information about diffusion anisotropy. While most studies focus on either the frequency-dependent [12] or tensorial [13] aspects of the encoding, Lundell et al. [54] proposed combining them into a unified multidimensional framework, about this we will introduce in the chapter 5.

4 Phantoms

When developing new MRI methods, one of the significant challenges is the validation and optimization of these methods. This involves validating pulse sequences, data processing pipelines, and implementing them on both preclinical and clinical MRI scanners. To accurately test the reliability and precision of our MRI processes, it is essential to design a diverse range of samples that accurately replicate the pathological conditions observed in biological tissues. These samples are commonly referred to as "phantoms" in MRI terminology. In this chapter, we will provide a more detailed explanation of the different phantoms used in this thesis.

4.1 Liquid crystal phantom

A phantom type composed of aqueous surfactant mixtures [55, 56] that can self-assemble into liquid crystalline phases with isotropic or anisotropic structures of different symmetries has been synthesized with varying microstructures [51, 57]. This section will introduce the basic knowledge of surfactants, the development of a lamellar liquid crystal phantom, and the characterization methods employed in this study.

4.1.1 Surfactants

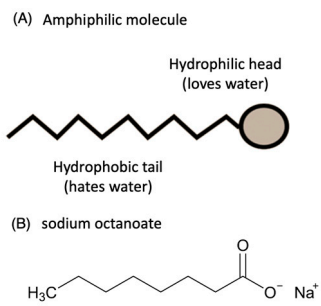

Figure 4.1: (A) Schematic illustration of a surfactant featuring a hydrophilic head and a hydrophobic tail. (B) The chemical structure of sodium octanoate, which was employed in this thesis.

Surfactants are a type of amphiphilic molecule, as depicted in Figure 4.1(A). They are composed of two parts: a hydrophilic head group that is attracted to water and a hydrophobic tail that repels water. Surfactants are commonly encountered in our everyday lives, present in products such as soaps and detergents. There are diverse types of surfactants, each exhibiting unique characteristics. The properties of a surfactant are primarily determined by the presence and type of charge carried by its head group. In Figure 4.1(B), we have specifically depicted chemical structure of sodium octanoate, which is utilized in this thesis.

4.1.2 Lyotropic liquid crystals

Lyotropic liquid crystals have a well-defined microstructure resembling that of a crystal. These liquid crystals are composed of two or more components that display liquid-crystalline properties within a specific concentration range. In the lyotropic phases, the constituents are enveloped by solvent molecules, which enhance the fluid nature of the system.

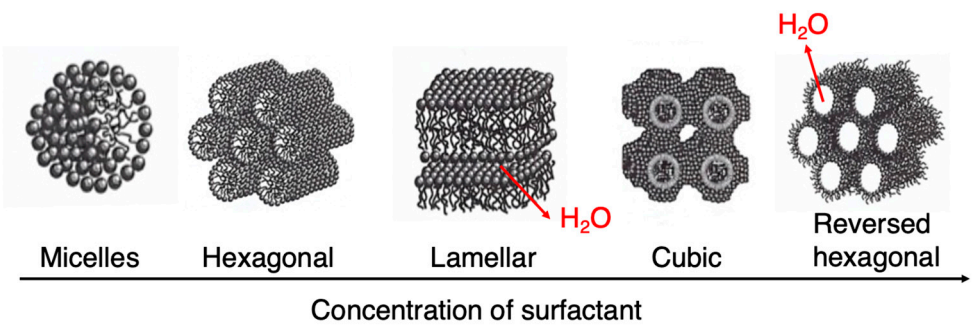

Figure 4.2: Liquid crystal structures under varying surfactant concentrations. The arrow indicates an increase in surfactant concentration, leading to the emergence of distinct structures. The illustrated liquid crystal structures from left to right are: Micelle, Hexagonal, Lamellar, Cubic, and Reverse hexagonal. These figures of liquid crystal structures were reproduced from reference [55].

Typically, lyotropic crystals consist of surfactants and water as their constituents. When surfactants are dissolved in water, their self-assembly can give rise to various liquid crystal structures. The specific structures formed depend on the concentration ratios of the constituents [55]. At very low surfactant concentrations, the surfactant molecules disperse randomly without any order. As the surfactant concentration increases, the molecules spontaneously assemble into micelles. Further increases in concentration lead to the successive emergence of the hexagonal phase, lamellar phase, and reversed hexagonal phase. Figure 4.2 illustrates some surfactant geometries, with the arrow in the diagram representing an increase in surfactant concentration, resulting in the formation of distinct structures. In these self-

assembled structures, the hydrophobic tails cluster together, while the hydrophilic head groups remain in contact with water. For example, in the lamellar phase, water moves between two surfactant bilayers, whereas in the reversed hexagonal phase, water moves along the axial direction. The formation of these structures is governed by the interactions between the surfactant components and water.

However, not all mixtures of surfactants and water can form all the mentioned in Figure 4.2. phases. To promote the formation of additional liquid crystal phases, the inclusion of a partially hydrophilic co-surfactant, such as this long-chain alcohol (1-decanol), is necessary. Figure 4.3 illustrates a three-component phase diagram, depicting an aqueous mixture of a sodium octanoate, 1-decanol, and water. The phase diagram consists of six different phases: two isotropic solution phases, three liquid crystalline phases, and a solid surfactant phase. It is worth noting that in binary mixtures with water, the surfactant forms only micelles and a hexagonal phase. The introduction of 1-decanol triggers a transition to the lamellar phase and at higher 1-decanol concentrations, to reversed structures such as and reversed hexagonal and reversed micellar phases [55].

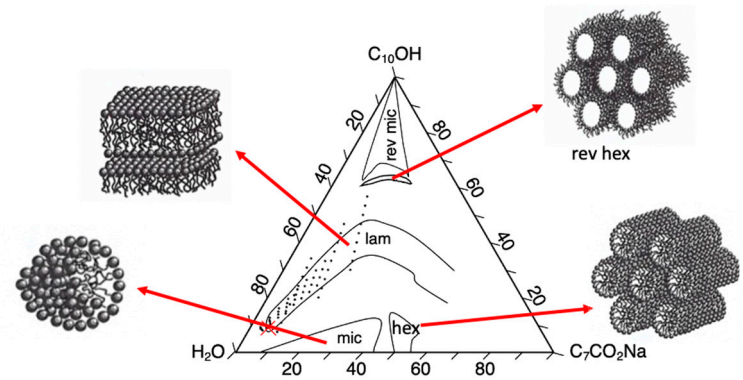

Figure 4.3: A ternary phase diagram of the sodium octanoate-decanol-water system at room temperature. The diagram exhibits two isotropic solution phases, namely micellar and reversed micellar phases, along with three liquid crystalline phases: hexagonal, lamellar, and reversed hexagonal phases.

Furthermore, lyotropic liquid crystals possess a crucial property where their self-assembled structures can be tuned by varying the concentration, even within the same phase. For example, in lamellar phases, the distance between two layers increases with an increase in water concentration. As shown in Figure 4.3, there are extremely broad regions with different concentrations that exhibit a pure lamellar phase. In this thesis, a lamellar liquid crystal was prepared by using the composition 85.79 wt% MilliQ, 9.17 wt% 1-decanol and 5.04 wt% sodium octanoate, the corresponding microstructure is a stack of surfactant bilayers intercalated by water, giving rise to a 2D anisotropic diffusion of water.

4.1.3 Polarized light microscopy for studying liquid crystals

Polarized light microscopy is a powerful technique used to distinguish between various microstructures of liquid crystals [58]. This method involves shining polarized light through a sample and observing how the light behaves as it passes through the material. When polarized light encounters anisotropic materials like liquid crystals, it can split into two rays with different refractive indices due to the material's molecular alignment. This phenomenon is known as birefringence. By analyzing the patterns and colours generated by the interaction of polarized light with liquid crystals, researchers can gain insights into the arrangement and orientation of the molecules within the sample.

Figure 4.4(A) illustrates a polarized light microscope configuration. This optical apparatus comprises a detector, lenses, and polarizing filters. The initial filter selects a specific light polarization, aligning the waves in a single direction. The second filter further refines this orientation. When the two filters are positioned perpendicular to each other, no light waves can pass through. Placing a sample in the light's path allows it to split into two rays with distinct delays if the sample is birefringent. The second filter only allows waves affected by the sample's polarization to pass, making the sample visible. For liquid crystal samples, transmitted waves undergo changes, affecting interference patterns after the second filter and altering the image's color.

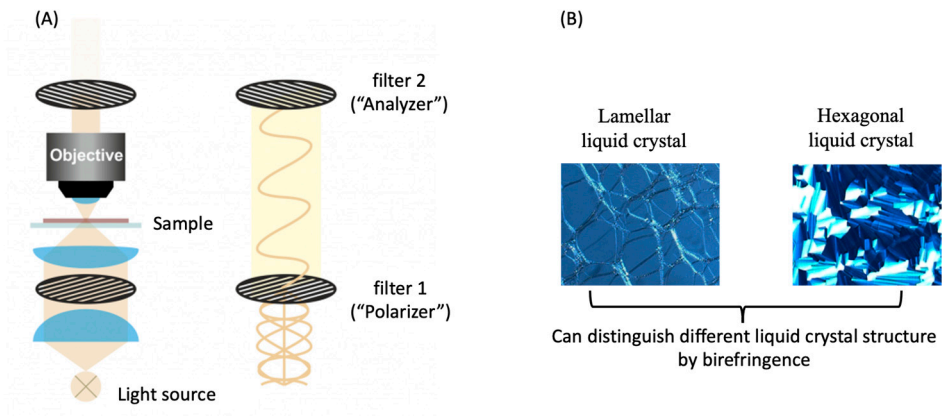

Figure 4.4: A schematic illustration of a polarized light microscope, and the textures of liquid crystals. (A) A diagram of a polarized light microscope, which consists of a detector, lenses, and two perpendicular polarizing filters, reproduced from ref. [59]. (B) Textures of lamellar and hexagonal liquid crystals observed through polarized light microscopy.

In cases of isotropic phases, the images from light microscopy appear black, whereas anisotropic phases generate bright images. Various anisotropic phases display unique patterns when observed through polarized light microscopy. Figure

4.4(B) provides visual examples of the characteristic textures found in lamellar and hexagonal liquid crystal phases [60]. Through analysis of images acquired via polarized light microscopy, it becomes feasible to identify the specific phases within samples, enabling differentiation between lamellar and hexagonal phases.

4.1.4 ^{2}H NMR spectroscopy to determine liquid crystals

Another very useful technique for determining surfactant phase behavior is NMR spectroscopy, specifically through the observation of quadrupole splitting in deuterium (^{2}H) NMR spectroscopy [55, 61]. This technique involves obtaining signals from either heavy water or deuterium-labeled surfactants. Different patterns observed in the ^{2}H spectra correspond to different phases, allowing for direct identification of the phases based on these spectra patterns.

The water-surfactant interface induces slight orientational anisotropy in the nearby water molecules. The orientational anisotropy can be detected as a quadrupole splitting in the ^{2}H spectrum of ^2H_2O. The expression for quadrupole splitting ($\Delta\upsilon_Q$) is given by [61]:

$$\Delta\upsilon_Q(\theta_{\mathbf{ml}}) = \frac{3}{2}\chi\overline{P_2(\cos\theta_{\mathbf{ml}})} \qquad (4.1)$$

where **l** is the direction of the externally applied magnetic field, **m** is the direction of the $^2\mathrm{H}-\mathrm{O}$ chemical bond, $\theta_{\mathbf{ml}}$ is the angle between **m** and **l**. χ is the quadrupole coupling constant, the value of χ is 254kHz in water [62]. $P_2(\cos\theta_{\mathbf{ml}}) = \frac{3(\cos\theta_{\mathbf{ml}})^2-1}{2}$ is the second Legendre polynomial.

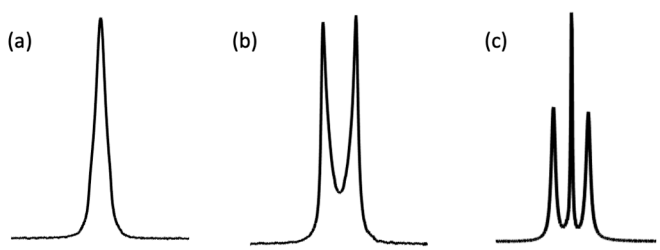

Figure 4.5: ^{2}H spectra patterns for different phases. (a) One isotropic phase. (b) One anisotropic phase. (c) One isotropic phase and one anisotropic phase [61].

Equation 4.1 indicates that $\Delta\upsilon_Q$ is proportional to the time average of $P_2(\cos\theta_{\mathbf{ml}})$. In cases of isotropic samples (such as micellar, sponge, cubic phases), the value of $\overline{P_2(\cos\theta_{\mathbf{ml}})}$ is zero, leading to no splitting and resulting in a narrow singlet in the spectrum. Conversely, for anisotropic samples, the interaction between the

surfactant and water causes water molecules in the immediate interface area to experience reorientation, introducing residual quadrupolar couplings and resulting in a non-zero value of $\overline{P_2(\cos\theta_{\mathbf{ml}})}$. As depicted in Figure 4.5, isotropic phases (micellar, sponge, or cubic) exhibit a narrow singlet, while anisotropic phases (hexagonal or lamellar) produce a doublet pattern [55].

4.2 Yeast cells

Yeat cells, known for their spherical shape, were used early as a model system to show the effect of restricted diffusion [63]. Additionally, yeast cells have been employed to validate double diffusion encoding (DDE) for achieving sensitivity to microscopic anisotropy [64]. In this case, the shape of the yeast cells was manipulated through irradiation and subsequent culturing, resulting in two samples of yeast cells with varying eccentricities. Both samples exhibited distinguishable differences in DDE signals acquired with co-linear and orthogonal gradient pairs. In recent experiments involving tensor-valued encoding, spherical yeast cells were utilized to create isotropic compartments within systems demonstrating intra-voxel variation in anisotropy [41, 65, 66].

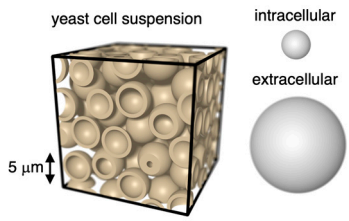

Figure 4.6: Microscopic structure of yeast cell suspension, depicting spherical shells representing cell membranes that separate intra- and extracellular water. The smaller and larger grey spheres on the right correspond to the intra- and extracellular water diffusion tensors. Figure is adapted with permission for ref. [41].

A yeast cell suspension was prepared by shaking equal volumes of fresh baker's yeast, purchased from a local supermarket, with tap water in a glass tube. The suspension was allowed to settle overnight at room temperature, and the clear supernatant was discarded. Figure 4.6 visually demonstrates the micrometer-scale structure of the yeast cell suspension, depicting spherical shells as cell membranes that separate the intra- and extracellular water compartments. In the cell suspension, two distinct water populations can be observed: intracellular (where water is confined within cells of approximately 5 μm in diameter) and extracellular (where water moves within the gaps between cells). Both populations exhibit isotropic diffusion, but with significant differences in apparent diffusivity. Within the scope

of this thesis, yeast cells were used as a sample to illustrate the effects of restricted diffusion in our recently developed encoding technique, which is double rotational encoding of the *q*-vector.

4.3 Brine solution

As shown in Figure 4.7, the phantoms were prepared to exhibit fast and slow isotropic gaussian diffusion. To mimic fast isotropic gaussian diffusion, pure water was utilized with a diffusion coefficient of approximately $2.3 \times 10^{-9} m^2/s$ at 25°C. For the preparation of the phantom with slow isotropic gaussian diffusion, a sample was obtained with only a single H_2O peak in the ^1H spectrum, but with a diffusion coefficient approximately five times slower than pure water. To achieve this, a concentrated magnesium nitrate ($Mg(NO_3)_2$) solution was prepared. The saturated solution of $Mg(NO_3)_2$ was found to yield the desired diffusion coefficient for H_2O, approximately $0.49 \times 10^{-9} m^2/s$ [67]. However, the T_2 value of the saturated $Mg(NO_3)_2$ solution was higher (around 500 ms) than the intended T_2 value (around 100 ms). To address this, a 0.27 wt% saturated cobalt nitrate ($Co(NO_3)_2$) solution was added to the saturated magnesium nitrate solution. This addition served to enhance the transverse relaxation of water protons in the solution by introducing paramagnetic dopants (Co^{2+}) [68].

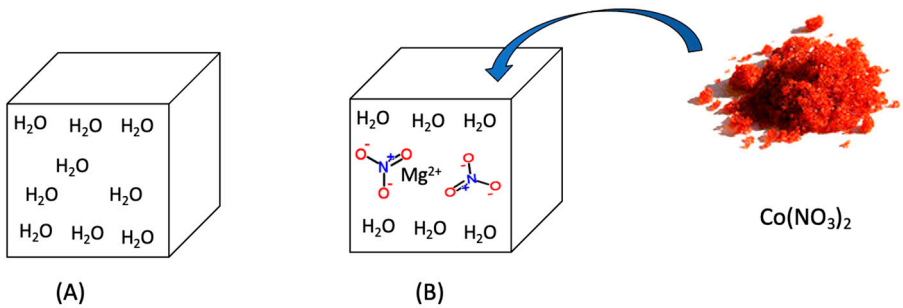

Figure 4.7: Phantoms with fast and slow isotropic Gaussion diffusion. (A) pure water. (B) "brine" concentrated magnesium nitrate solution in water, to enhance the transverse relaxation of water proton in the solution by introducing paramagnetic dopants (Co^{2+}).

5 Advanced diffusion encoding

Temporal variations in magnetic field gradients give rise a phenomenon that makes the MRI signal sensitive to molecular motion, including bulk diffusion, flow, time and frequency dependence ("restriction"), anisotropy, and exchange. The commonly used pulsed gradient spin-echo sequence can provide information about all these aspects. However, there has been a recent increase in interest in understanding how MRI can investigate specific characteristics of stochastic processes. Advanced diffusion MRI methods incorporating specialized diffusion encoding schemes have shown potential for clinical research applications [69]. Notable examples include using oscillating gradients to estimate cell sizes [10, 32] and tensor-valued encoding to characterize cell shapes [11] in breast tumors. Lundell et al. [54] proposed combining them into a unified multidimensional framework. This approach was demonstrated using gradient waveforms derived from the magic angle spinning (MAS) technique in solid-state NMR spectroscopy [70, 71]. In the following, we will introduce the magic angle spinning of the q-vector method and then present the design of gradient waveforms using the "double-rotation" technique, enabling comprehensive exploration of the 2D frequency-anisotropy space.

5.1 Magic angle and variable angle spinning of the q-vector

At certain specific frequency values, an axially symmetric tensor-valued encoding spectrum $\mathbf{b}(\omega)$ - simplified as the frequency-independent diffusion encoding tensor denoted as **b**-tensor - can be acquired by choosing a q-vector trajectory. In particular, the **q** unit vector ($\mathbf{n}(t)$) in equation 3.20 is calculated by rotating the initial unit vector $\mathbf{n}(0) = [0, 0, 1]^{\mathrm{T}}$. The unit vector trajectory is expressed as:

$$\mathbf{n}(t) = \mathbf{R}_z(\psi(t))\mathbf{R}_y(\xi)\ [0, 0, 1]^{\mathrm{T}}. \qquad (5.1)$$

here, $\mathbf{R}_z$ and $\mathbf{R}_y$ are Euler rotation matrices, ζ is the inclination angle of the q-vector relative to the z-axis, and ψ is the time-dependent azimuthal angle of rotation about the z-axis increases from 0 to 2π during the time t from 0 to τ. The unit vector trajectories are then converted into q-vector trajectories $q_i(t)$ and gradient

waveforms $g_i(t)$, as detailed in previous work [70, 71]. The trace of the **b**-tensor is denoted as b, calculated using equation 3.22. The anisotropy of **b**-tensor, referred to as b_Δ ("shape"), is determined by the polar angle ζ, as described in [57]:

$$b_\Delta = P_2(\cos\zeta), \tag{5.2}$$

where $P_2(\cos\zeta)$ is the second-order Legendre polynomial,

$$P_2(\cos\zeta) = \frac{3\cos^2\zeta - 1}{2}. \tag{5.3}$$

At the magic angle $\zeta = \theta_m \cong 54.7°$, $P_2(\cos\theta_m) = \frac{3\cos^2\theta_m - 1}{2} = 0$. This signifies that isotropic diffusion encoding is achieved by maintaining the q-vector at a constant inclination angle equal to the magic angle, as depicted in Figure 5.1 (A). This isotropic diffusion encoding leads to signal attenuation where the anisotropic contribution diminishes, in contrast to the signal attenuation observed in conventional diffusion encoding where both isotropic and anisotropic contributions play a role. The distinct signal patterns produced by these two different diffusion encodings allow for the differentiation of microscopic structures when anisotropic components are present [70, 71].

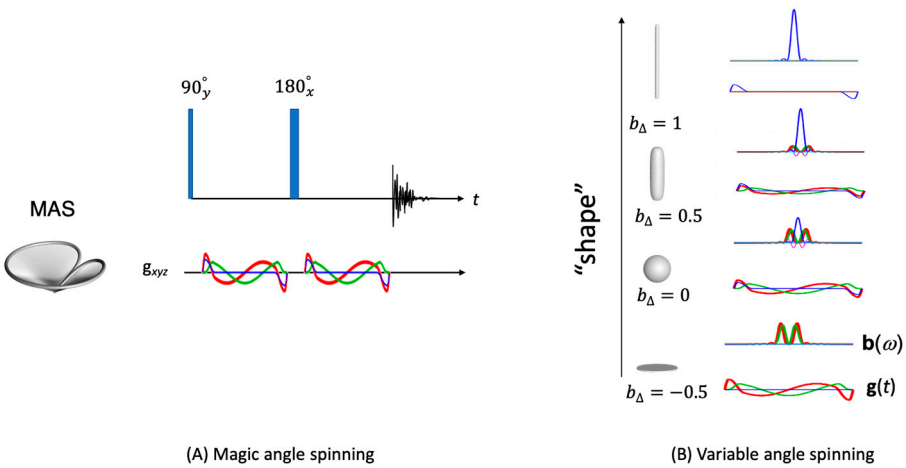

Figure 5.1: Spin-echo with MAS encoding and variable angle spinning. (A) A schematic of the spin-echo with MAS encoding is presented, illustrating smooth modulated gradients *x*, *y*, and *z* in red, green, and blue, respectively, which is an isotropic diffusion encoding. The corresponding 3D MAS *q*-vector trajectory is also shown (left). (B) Different shapes (b_Δ) achieved through variable angle spinning are presented, accompanied by their corresponding tensor-valued encoding spectrum $b(\omega)$ and gradient waveforms. Superquadric tensor glyphs along the vertical axis illustrate the **b**-tensor for selected b_Δ.values.

Altering the inclination angle ζ yields various shapes of **b**-tensors, illustrated in Figure 5.1 (B) along with the gradient waveforms $g_i(t)$ and corresponding tensor-valued encoding spectrum $\mathbf{b}(\omega)$. Superquadric tensor glyphs [29] along the vertical axis depict **b** for chosen b_Δ values, with the corresponding ζ obtained using equation 5.2.

Magic angle and variable angle spinning of the q-vector provides the gradient waveforms $g_i(t)$ for certain specific frequency values ω_{cent} and the normalized anisotropy b_Δ ("shape"), which can detect the effects of shape **D**-tensors (D_Δ as depicted in Figure 2.5) [41, 66].

5.2 Double rotation of the q-vector

Building on theory from magic-angle spinning [70] and variable-angle spinning [57], recently suggested double rotation (DOR) for comprehensive analysis of restricted-anisotropic self-diffusion system [53]. DOR unit vector trajectories were calculated by subjecting the vector $\mathbf{n}(0) = [0, 0, 1]^T$ to a series of rotations (from right to left) $\mathbf{R}_z(\psi_2)\mathbf{R}_y(\zeta_2)\mathbf{R}_z(\psi_1)\mathbf{R}_y(\zeta_1)$, where $\zeta_1 = \pi/2$ and $\zeta_2 = \theta_m \cong 54.7°$ are the inclinations of the two rotation axes. The time-dependent angles of rotation ψ_1 and ψ_2 about the two axes are coupled by the relation $\psi_1 = n\psi_2$, where n is an integer and ψ_2 increases from 0 to 2π during the time t from 0 to τ. For more detailed derivation regarding DOR, please refer to paper II. Figure 5.2 presents the q-vector trajectories of the double rotation (DORn) technique and the corresponding gradient waveforms $g_i(t)$ with centroid frequency ω_{cent} for the cases where $b_\Delta = 0$. Combining with Figure 5.1 B, DORn provides the gradient waveforms $g_i(t)$ for comprehensive sampling of the 2D space consisting of the centroid frequency ω_{cent} and the normalized anisotropy b_Δ ("shape") of the encoding tensor $\mathbf{b}(\omega)$ with elements $b_{ij}(\omega)$, these variables have been defined through the equations 3.27-3.31.

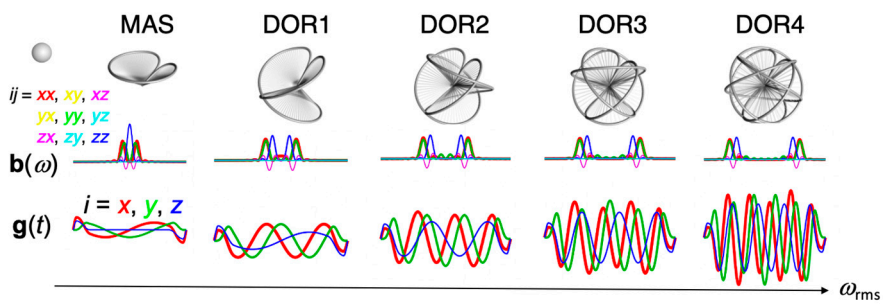

Figure 5.2: Double rotation (DORn) encoding with increasing centroid frequency ω_{cent} for the $b_\Delta = 0$ cases. From the top to bottom: 3D plots q-vector trajectories(top), corresponding tensor-valued encoding spectrum $\mathbf{b}(\omega)$(middle) and gradient waveforms $g_i(t)$ (bottom).

The ability of the new gradient waveforms to give access to the complete 2D $\omega_{cent}-b_\Delta$ plane is demonstrated by microimaging measurements in the chapter 3 introduced phantoms with well-defined restriction and anisotropy properties, namely and concentrated salt solution with isotropic Gaussian diffusion, a lamellar liquid crystal giving anisotropic Gaussian diffusion, and a yeast cell sediment exhibiting isotropic restricted diffusion.

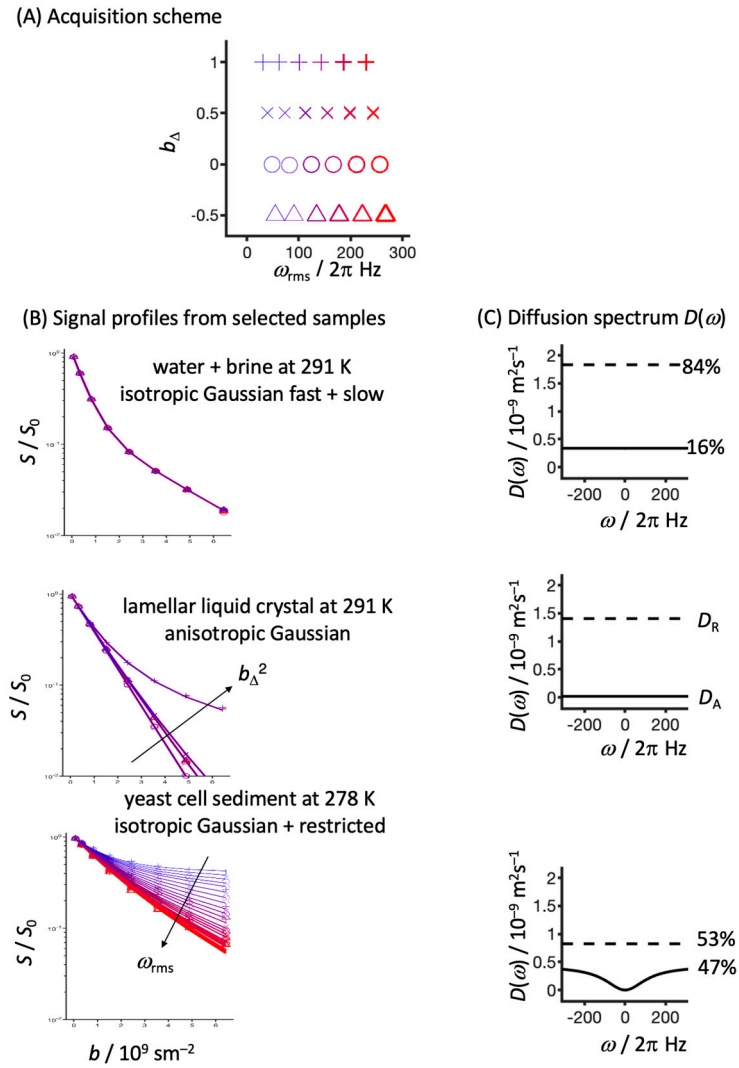

Figure 5.3: Demonstration of DOR encoding methods on different phantoms. (A) Data acquisition setup: data were acquired for 8 b values up to 6.44×10^9 s m^{-2} and 15 orientations. For each of these settings, the 2D ω_{cent} values (different colors) and b_Δ values (marker style) corresponded to the gradient waveforms by DOR methods. (B) Signal profiles from selected samples: experimental (markers) and fitted (line) normalized powder-averaged signal S/S_0 plotted against the b value for phantoms with well-defined

diffusion properties. From top to bottom, the samples are as follows: tube-in-tube assembly of pure water and a concentrated solution of magnesium nitrate in water ("brine"), resulting in two isotropic Gaussian (ω-independent) components; Polydomain lamellar liquid crystal showing Gaussian parallel and perpendicular diffusivities, $D_{\parallel}$ and $D_{\perp}$; Sediment of yeast cells with intracellular (restricted diffusion) and extracellular (isotropic Gaussian diffusion) compartments. (C) Diffusion spectrum $D(\omega)$ results for the corresponding phantoms.

Figure 5.3 presents the results of experimental data and corresponding fits for all examined samples. The results are depicted in $\log_{10}(S)$ vs. b plots, where different marker styles and colors represent variations in dimensions b_{Δ} and ω_{cent}. The experimental data are illustrated within the Figure 5.3. The alignment of all data points onto a single master curve in the $\log_{10}(S)$ vs. b plot for the isotropic Gaussian phantom confirms consistent b-values obtained from all 24 waveforms used to sample the 2D (b_{Δ}, ω_{cent}) space. In the case of the anisotropic Gaussian phantom, the signal remains unaffected by ω_{cent} but exhibits a strong dependence on b_{Δ}, fitting well with the expression applicable to randomly oriented axisymmetric diffusion tensors [51]. For the isotropic restriction yeast cell phantom, the behaviour of the signal is notably affected by ω_{cent}, in alignment with the diffusion spectrum $D(\omega)$ associated with spherical restriction [20]. It's worth noting that for the isotropic restricted, even though it may seem to have a dependency on b_{Δ}, the data points do not clearly segregate into distinct master curves due to the interaction between b_{Δ} and ω_{cent}. Figure 5.3(A) illustrates the 24 investigated values in the 2D b_{Δ}-ω_{cent} space, revealing an actual alteration in the sampling grid ω_{cent} linked to each b_{Δ}. The slight correlation between b_{Δ} and ω_{cent} is indeed a drawback of our current waveform generation approach. However, despite this drawback, the signal obtained from isotropic restricted and Gaussian components fits the acquired data extremely well, indicating that the data's behaviour is not dependent on the value of b_{Δ}. The resulting diffusivities are consistent with previous findings for intra- and extracellular water in yeast cell sediments [72].
In conclusion, the data presented in Figure 5.3 validate that the set of waveforms allows for a thorough exploration of the 2D b_{Δ}-ω_{cent} space in the context of multidimensional diffusion encoding.

6 Model-free quantitative metrics

The integration of oscillating gradients and tensor-valued encoding within a single data collection process is driving the development of a cohesive approach to analyse the data. Drawing inspiration from the methods used to study the rotational dynamics of macromolecules through NMR [73], a technique known as "Model-free," we have formulated a method to effectively report specific microstructural details of biological tissues using quantitative metrics. These metrics are not reliant on specific models. This approach is based on the existing nonparametric diffusion tensor distributions [74], which are then enhanced by incorporating a novel measurement related to frequencies-Lorentzian frequency dimension.

In this section, we will initially introduce the concept of the model-free approach. Subsequently, we will demonstrate how we tested this approach on well-defined samples to ensure its reliability. Lastly, we will present the outcomes we obtained when applying this method to biological tissues.

6.1 Model-free approach

The concept of the model-free approach originates from the notion of deriving an analytical strategy without relying on any specific model for data analysis. This approach was initially introduced in the context of interpreting NMR relaxation experiments on macromolecules in solution by Lipari and Szabo [73]. In this framework, the dynamics information captured in relaxation experiments is succinctly characterized by two fundamental parameters: (1) a generalized order parameter denoted as S, which quantifies the degree of spatial restriction of motion, and (2) an effective correlation time, τ_e, which signifies the rate of motion. The corresponding spectral density is mathematically expressed as [73]:

$$J(\omega) = \frac{2}{5}\left(\frac{S^2\tau_M}{1+(\tau_M\omega)^2} + \frac{(1-S^2)\tau}{1+(\tau\omega)^2}\right), \tag{6.1}$$

where

$$\tau^{-1} = {\tau_M}^{-1} + {\tau_e}^{-1}. \tag{6.2}$$

here, τ_M represents the overall motion correlation time.

This approach is termed "model-free" because the spectral density derived from equation 6.1 is constructed without invoking a specific model for internal motions, because the parameters S and τ_M are defined in a model-independent manner. The experimental relaxation data were fitted using a least-squares approach with equation 6.1, with S^2 and τ_e considered as the only adjustable parameters. Numerical values for S^2 and τ_e can then be obtained through the fitting of experimental relaxation data. Subsequently, we can interpret the corresponding motion within the framework of a specific model based on the derived S^2 and τ_e values. This approach's logic differs from the traditional method, where the spectral density is evaluated based on a pre-established model structure. Instead, here, the analysis of data does not rely on a predetermined model structure; the system's motion model is determined based on the obtained parameters.

We introduce the "model-free" approach to estimate nonparametric $\mathbf{D}(\omega)$-distributions by global inversion of data acquired as $\mathbf{b}(\omega)$-encoded, quantify the restricted and anisotropic diffusion of water within heterogeneous biological tissues, employing nonparametric distributions of tensor-valued Lorentzians [20, 45]. Specifically, for heterogeneous systems comprised of multiple sub-ensembles, ensembles of discrete $\mathbf{D}(\omega)$-distributions are estimated for each set of $\mathbf{b}(\omega)$-encoded signals via Monte Carlo inversion [75]. In the principal axis system, axially symmetric $\mathbf{D}(\omega)$ is characterized by frequency-dependent axial and radial eigenvalues, $D_A(\omega)$ and $D_R(\omega)$, which are described using Lorentzian transitions between the zero-frequency values, D_A and D_R:

$$D_{A/R}(\omega) = D_0 - \frac{D_0 - D_{A/R}}{1+\omega^2/\Gamma_{A/R}^2}. \tag{6.3}$$

here, D_0 represents the high-frequency isotropic diffusivity, while Γ_A and Γ_R denote the frequencies at the centres of the transitions. In the lab frame, $\mathbf{D}(\omega)$ is given by

$$\mathbf{D}(\omega) = \mathbf{R}(\theta,\phi) \cdot \mathbf{D}^{PAS}(\omega) \cdot \mathbf{R}^{-1}(\theta,\phi). \tag{6.4}$$

where θ and ϕ are polar and azimuthal angles, $\mathbf{R}(\theta, \phi)$ is a rotation matrix. The sub-ensemble $\mathbf{D}(\omega)$-distribution information obtained from experiments can be comprehensively described by the statistical weight w and the parameter set [D_A, D_R, θ, ϕ, D_0, Γ_A, Γ_R].

The $D_A(\omega)$ and $D_R(\omega)$, as defined in equation 6.3, is derived without relying on specific diffusion models (like restricted, isotropic, or anisotropic diffusion), we just impose sensible limitations on the elements of the $\mathbf{D}(\omega)$-distributions, which involves that the ω-dependence of tensor eigenvalues follow a Lorentzian pattern [20, 45] and tensor shapes are axisymmetric [51]. As a result, the associated

statistical weight w and the parameter set [D_A, D_R, θ, ϕ, D_0, Γ_A, Γ_R] remain free from predefined models. The values for w and the set [D_A, D_R, θ, ϕ, D_0, Γ_A, Γ_R] for each sub-ensemble can be obtained from the data. This helps us figure out what types of diffusion exist in the samples we're studying, and how they are spread out. This gives us insight into new information about the structures we didn't know about before. It's a useful way to discover small-scale structures in living tissues that we hadn't seen previously.

The proposed methodology is validated through various experiments, including phantom validation, studies on ex vivo mouse brain tissue and tumor tissues. Subsequent sections will present the corresponding outcomes obtained from different samples.

6.2 Phantom validation

For visualization purposes, the $\mathbf{D}(\omega)$-distributions in the primary analysis space [D_A, D_R, θ,ϕ, D_0, Γ_A, Γ_R] are assessed at specific ω values using equation 6.3, resulting in [$D_A(\omega)$, $D_R(\omega)$, θ, ϕ,], and projected onto the dimensions of isotropic diffusivity $D_{iso}(\omega)$ and squared normalized anisotropy $D_\Delta(\omega)$ through the following equations:

$$D_{iso}(\omega) = \frac{D_A(\omega)+2D_R(\omega)}{3}. \quad (6.5)$$

and

$$D_\Delta(\omega)^2 = \frac{[D_A(\omega)-D_R(\omega)]^2}{[D_A(\omega)+2D_R(\omega)]^2}. \quad (6.6)$$

Experimental validation of this approach is presented in Figure 6.1 using two samples with well-defined restriction and anisotropy properties: a yeast cell sediment and an assembly of glass tubes containing pure water, saturated salt solution, and lamellar liquid crystal. These qualitative observations of restriction and anisotropy from the raw signal data are further elaborated upon and detailed through the obtained $\mathbf{D}(\omega)$-distributions. The yeast sample comprises two isotropic ($D_\Delta(\omega) = 0$) pools, one Gaussian (ω-independent) and one restricted (ω-dependent) originating respectively from the extracellular and intracellular spaces separated by nearly impermeable plasma membranes [76]. The composite phantom exhibits three Gaussian pools, one of which is anisotropic with a $D_\Delta(\omega)$ value of 0.25, consistent with the essentially two-dimensional diffusion of water confined to the nanometre-scale gaps between the planar detergent bilayers in a lamellar liquid crystal [57]. The sensitivity to $\omega_{cent}/2\pi$ in the examined range of 20-260 Hz for the yeast cell

sediment suggests restriction within micrometre-scale compartments, while the dependency on b_Δ for the composite phantom reveals anisotropy.

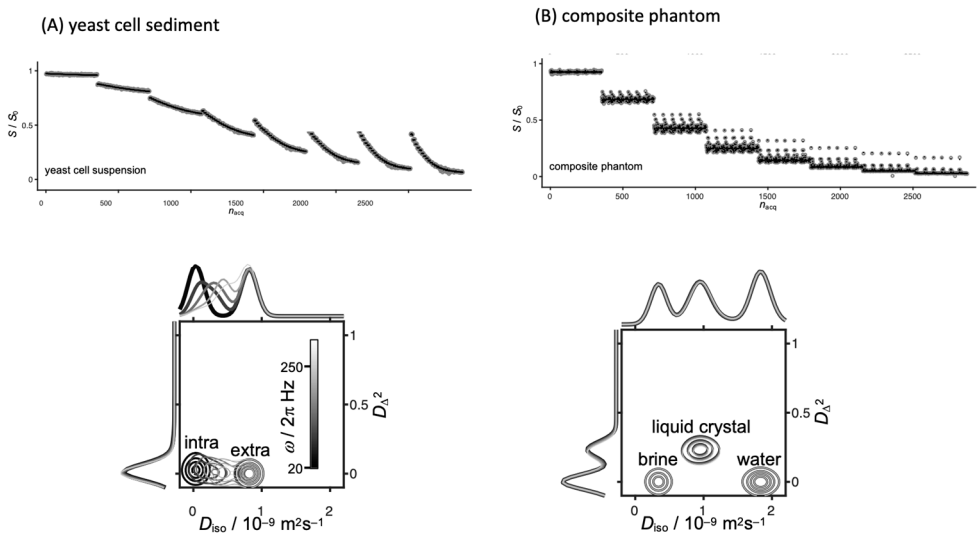

Figure 6.1: $\mathbf{D}(\omega)$ distributions obtained through Monte Carlo inversions of $b(\omega)$ −encoded signals on Phantoms. (A) The results from a yeast cell sediment. (B) The outcomes from a composite phantom containing glass tubes filled with diverse substances, including pure water, a magnesium nitrate-saturated solution (brine), and a lamellar liquid crystal. These $\mathbf{D}(\omega)$-distributions are projected onto the 2D plane and 1D axes representing isotropic diffusivity (D_{iso}) and squared normalized anisotropy (D_Δ^2) for five specific ω values, visualized using a linear grayscale of contour lines. It's important to note that while the intracellular water within the yeast displays ω dependent restricted behavior, the other four water pools demonstrate Gaussian behavior that remains unaffected by ω within the examined ω /2π range of 20 to 260 Hz.

6.3 Quantitative assessment of biological tissues

Illustration of the proposed method's application to quantify microstructural properties within biological tissues, including *ex vivo* rat brain and excised tissue from a xenograft model of neuroblastoma [77].

To derive parameter maps, the extensive data within the $\mathbf{D}(\omega)$-distributions is summarized by computing the means E[x], variances Var[x], and covariances Cov[x,y] across relevant dimensions and segmented divisions ("bins") of the distribution space [74, 78].

Although the $\mathbf{D}(\omega)$-distributions cover a wide range of ω values, our encoding process has primarily concentrated on investigating the more limited span between the minimum and maximum ω_{cent} values. This specific range holds particular importance for interpretation. Building upon previous research utilizing oscillating

gradient encoding [48, 79, 80], we measure the impact of restriction by quantifying the finite difference approximation of metric changes within the examined frequency window.

$$\Delta_{\omega/2\pi}\mathrm{E}[D_{\mathrm{iso}}] = \frac{\mathrm{E}[D_{\mathrm{iso}}(\omega_{\max})] - \mathrm{E}[D_{\mathrm{iso}}(\omega_{\min})]}{(\omega_{\max} - \omega_{\min})/2\pi} \qquad (6.7)$$

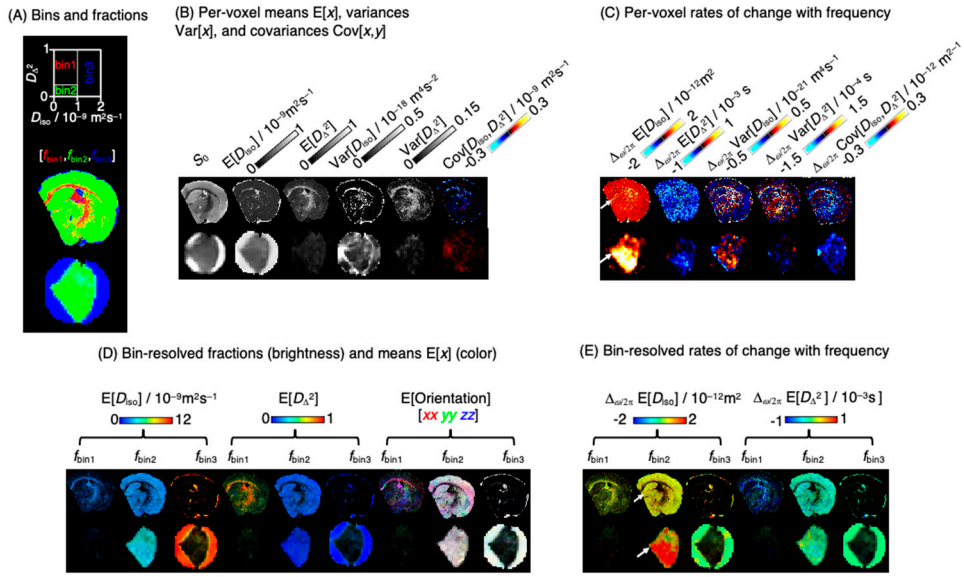

Figure 6.1: Parameter maps derived from the per-voxel $\mathbf{D}(\omega)$ distributions obtained for *ex*-vivo rat brain and tumor tissues. (A) Definition of bins in the 2D D_{iso}- D_{Δ}^2 projection, and visualization of per-bin signal fractions [f_{bin1},f_{bin2},f_{bin3}] indicated by color. (B) Statistical descriptors E[*x*], Var[*x*], and Cov[*x*,*y*] presented across the D_{iso} and D_{Δ}^2 dimensions of the $\mathbf{D}(\omega)$-distributions ($\omega/2\pi$ = 53 Hz). (C) Depiction of frequency-induced rate changes, $\Delta_{\omega/2\pi}$ for per-voxel. (D) Bin-resolved signal fractions and means E[*x*] for diffusion metrics at $\omega/2\pi$ = 53 Hz, represented through a blue-green-red color scale on the horizontal axis. Orientation color-coding is derived from lab-frame diagonal values [D_{xx},D_{yy},D_{zz}] normalized by the maximum eigenvalue D_{33}. (E) Bin-resolved rates of frequency-induced changes.

Figure 6.1 presents a compilation of maps showcasing statistical descriptors E[D_{iso}], E[D_{Δ}^2], Var[D_{iso}], Var[D_{Δ}^2], and Cov[D_{iso},D_{Δ}^2] on a per-voxel and bin-resolved basis for rat brain and tumor tissues. These descriptors are typically associated with tensor-valued encoding [69, 74] and provide insights into the (rates of) changes in diffusivity metrics with frequency, including $\Delta_{\omega/2\pi}\mathrm{E}[D_{\mathrm{iso}}]$,which is used to visualize oscillating gradient encoding results [48, 79, 80]. Additionally, novel metrics that correlate information about restriction and anisotropy are also presented.

A noteworthy aspect in the case of rat brain tissue is the distinction between high- and low- D_{Δ}^2 components with similar D_{iso} values (bin1 and bin2). Furthermore, the

effects of restricted diffusion are linked to the low- D_{Δ}^{2} component (bin2) as depicted in Figure 6.1(E).

The maps of the excised tumor display a region characterized by significant restricted diffusion effects (high $\Delta_{\omega/2\pi}\mathrm{E}[D_{\mathrm{iso}}]$). Additionally, there are areas showing elevated Var[D_{iso}], attributed to the presence of both low- and high- D_{iso} water compartments within the same imaging voxel. This occurrence might stem from factors including densely populated tumor regions, the presence of formaldehyde solution, or tissues with compromised membranes.

Our study has shown that the successful fitting of experimental data and achieve expected outcomes. However, it's important to highlight that our simplified model is based on mathematical expressions for restricted diffusion in confined spaces, as described in Paper III of the methods section. We've worked to find a good balance between being physically accurate, mathematically practical, and useful for real-world applications, while also avoiding making overly complex interpretations. Our approach involves using specific mathematical components and techniques, like tensor-valued Lorentzian functions and Monte Carlo analysis, to extract valuable insights from the data without adding unnecessary confusion.

7 Concluding remarks

In conclusion, this Ph.D. thesis introduces a novel diffusion MRI framework designed to unravel and characterize microscopic tissue environments across the multidimensional space of anisotropic and restricted diffusion. Inspired by signal encoding techniques in solid-state NMR and data inversion strategies in macromolecular rotational dynamics, we developed innovative acquisition and analysis protocols. This signal encoding novel approach generates a flexible family of modulated gradient waveforms, allowing for comprehensive exploration of the 2D frequency-anisotropy space, and the data inversion strategy yields model-independent quantitative metrics, facilitating the inversion of experimental data obtained through the novel signal encoding technique. This innovative diffusion MRI framework holds promise for assessing microstructural properties in heterogeneous tissues with distinct anisotropy and restriction attributes.

The development of this protocol unfolded across multiple papers, phantom development (Paper I), addressing new signal encoding theory (Paper II), theoretical establishment of data inversion (Paper III), and application in in vivo studies (Paper IV). The individual conclusions from these papers are summarized as follows:

Paper I: The study demonstrates a successful method for creating a lamellar liquid crystal phantom that mimics diffusive properties of layered structures found in intracranial tumors. The phantom, tailored for whole-body MRI, primarily consists of pure lamellar regions, enabling validation of new diffusion MRI techniques for assessing layered microstructures in the brain.

Paper II: Our approach employs advanced motion-encoding gradients that flexibly detect both restricted and anisotropic diffusion within a unified multidimensional framework. The proposed double-rotation gradient waveforms enable comprehensive sampling of both the frequency and "shape" dimensions of diffusion encoding, crucial for detailed characterization of restriction and anisotropy in materials like brain tissues. These waveforms, derived from simple geometry and expressed through compact mathematics, are suitable for preclinical investigations and can potentially be adapted for human in vivo studies through numerical optimizations.

Paper III: Through establishing connections between NMR analysis of rotational dynamics in macromolecules and diffusion MRI in biological tissues, we formulated model-free analysis strategies. These strategies enable the examination of data using

the data acquisition method described in Paper II. To illustrate the practicality of this approach, we employed it on MRI phantoms containing various well-defined water pools, including the lamellar liquid crystal phantom developed in Paper I. This work represents a significant step towards model-free investigations of restriction and anisotropy in heterogeneous biological tissues, with implications for understanding microstructural changes associated with pathology or normal brain development.

Paper IV: Incorporating diffusion frequency in multidimensional diffusion-relaxation correlation MRI enables better depiction of diffusion signals in tissues such as gray matter and tumors. This approach facilitates correlation between frequency-dependent diffusion and diffusion shape, diffusivity, orientations, and relaxation rates. It offers broader applicability and avoids overestimation of diffusivity and micro-anisotropy, even in the case of restricted diffusion behavior.

Our experimentation with phantoms, ex vivo rat brains, and tissue sample from human tumors has effectively showcased the adaptability and practicality of our innovative diffusion MRI approach in capturing microstructural properties. This breakthrough not only opens new prospect for investigating intricate multi-component tissues within both tumors and healthy brains but also lays the foundation for potential clinical applications. Moving forward, the next step involves further refining our encoding protocol to optimize its performance and suitability, paving the way for its eventual application on clinical scanner.

References

[1] I. Zemmoura, E. Blanchard, P.-I. Raynal, C. Rousselot-Denis, C. Destrieux, S. Velut, How Klingler's dissection permits exploration of brain structural connectivity? An electron microscopy study of human white matter, Brain Structure and Function, 221 (2016) 2477-2486.

[2] X.-B. Liu, C.M. Schumann, Optimization of electron microscopy for human brains with long-term fixation and fixed-frozen sections, Acta neuropathologica communications, 2 (2014) 1-10.

[3] W.S. Price, NMR studies of translational motion, Cambridge, 2009.

[4] P.T. Callaghan, Translational dynamics and magnetic resonance: principles of pulsed gradient spin echo NMR, Oxford University Press, 2011.

[5] E.O. Stejskal, J.E. Tanner, Spin diffusion measurements: spin echoes in the presence of a time-dependent field gradient, The journal of chemical physics, 42 (1965) 288-292.

[6] L. Filidoro, O. Dietrich, J. Weber, E. Rauch, T. Oerther, M. Wick, M. Reiser, C. Glaser, High-resolution diffusion tensor imaging of human patellar cartilage: feasibility and preliminary findings, Magnetic Resonance in Medicine: An Official Journal of the International Society for Magnetic Resonance in Medicine, 53 (2005) 993-998.

[7] T.L. Chenevert, J.A. Brunberg, J.G. Pipe, Anisotropic diffusion in human white matter: demonstration with MR techniques in vivo, Radiology, 177 (1990) 401-405.

[8] C. Beaulieu, The basis of anisotropic water diffusion in the nervous system–a technical review, NMR in Biomedicine: An International Journal Devoted to the Development and Application of Magnetic Resonance In Vivo, 15 (2002) 435-455.

[9] P.J. Basser, C. Pierpaoli, Microstructural and physiological features of tissues elucidated by quantitative-diffusion-tensor MRI, Journal of magnetic resonance, 213 (2011) 560-570.

[10] J. Xu, X. Jiang, S.P. Devan, L.R. Arlinghaus, E.T. McKinley, J. Xie, Z. Zu, Q. Wang, A.B. Chakravarthy, Y. Wang, MRI-cytometry: mapping nonparametric cell size distributions using diffusion MRI, Magnetic resonance in medicine, 85 (2021) 748-761.

[11] I.D. Naranjo, A. Reymbaut, P. Brynolfsson, R. Lo Gullo, K. Bryskhe, D. Topgaard, D.D. Giri, J.S. Reiner, S.B. Thakur, K. Pinker-Domenig, Multidimensional diffusion magnetic resonance imaging for characterization of tissue microstructure in breast cancer patients: a prospective pilot study, Cancers, 13 (2021) 1606.

[12] M. Aggarwal, Restricted diffusion and spectral content of the gradient waveforms, Advanced Diffusion Encoding Methods in MRI, edited by: Topgaard, D., Royal Society of Chemistry, Cambridge, UK, (2020) 103-122.

[13] A. Reymbaut, Diffusion anisotropy and tensor-valued encoding, Advanced Diffusion Encoding Methods in MRI, 4 (2020) 68.

[14] H.J.V. Tyrrell, K. Harris, Diffusion in liquids: a theoretical and experimental study, Butterworth-Heinemann, 2013.

[15] B.E. Poling, J.M. Prausnitz, J.P. O'connell, Properties of gases and liquids, McGraw-Hill Education, 2001.

[16] E.L. Cussler, Diffusion: mass transfer in fluid systems, Cambridge university press, 2009.

[17] R.B. Bird, Transport phenomena, Appl. Mech. Rev., 55 (2002) R1-R4.

[18] P. Linse, O. Soderman, The validity of the short-gradient-pulse approximation in NMR studies of restricted diffusion. Simulations of molecules diffusing between planes, in cylinders and spheres, Journal of Magnetic Resonance, Series A, 116 (1995) 77-86.

[19] P.T. Callaghan, Pulsed-gradient spin-echo NMR for planar, cylindrical, and spherical pores under conditions of wall relaxation, Journal of magnetic resonance, Series A, 113 (1995) 53-59.

[20] J. Stepišnik, Time-dependent self-diffusion by NMR spin-echo, Physica B: Condensed Matter, 183 (1993) 343-350.

[21] A. Klemm, R. Metzler, R. Kimmich, Diffusion on random-site percolation clusters: Theory and NMR microscopy experiments with model objects, Physical Review E, 65 (2002) 021112.

[22] E.G. Novikov, D. van Dusschoten, H. Van As, Modeling of self-diffusion and relaxation time NMR in multi-compartment systems, Journal of Magnetic Resonance, 135 (1998) 522-528.

[23] L. van der Weerd, S.M. Melnikov, F.J. Vergeldt, E.G. Novikov, H. Van As, Modelling of self-diffusion and relaxation time NMR in multicompartment systems with cylindrical geometry, Journal of Magnetic Resonance, 156 (2002) 213-221.

[24] G.E. Uhlenbeck, L.S. Ornstein, On the theory of the Brownian motion, Physical review, 36 (1930) 823.

[25] P.J. Basser, J. Mattiello, D. LeBihan, MR diffusion tensor spectroscopy and imaging, Biophysical journal, 66 (1994) 259-267.

[26] D. Topgaard, NMR methods for studying microscopic diffusion anisotropy, Diffusion NMR in Confined, (2016) 226-259.

[27] C.-F. Westin, H. Knutsson, O. Pasternak, F. Szczepankiewicz, E. Özarslan, D. van Westen, C. Mattisson, M. Bogren, L.J. O'Donnell, M. Kubicki, Q-space trajectory imaging for multidimensional diffusion MRI of the human brain, Neuroimage, 135 (2016) 345-362.

[28] D. Topgaard, O. Söderman, Self-diffusion in two-and three-dimensional powders of anisotropic domains: An NMR study of the diffusion of water in cellulose and starch, The Journal of Physical Chemistry B, 106 (2002) 11887-11892.

[29] G. Kindlmann, Superquadric tensor glyphs, in: Proceedings of the Sixth Joint Eurographics-IEEE TCVG conference on Visualization, 2004, pp. 147-154.

[30] H. Li, X. Jiang, F. Wang, J. Xu, J.C. Gore, Structural information revealed by the dispersion of ADC with frequency, Magnetic resonance imaging, 33 (2015) 1083-1090.

[31] H. Li, J.C. Gore, J. Xu, Fast and robust measurement of microstructural dimensions using temporal diffusion spectroscopy, Journal of magnetic resonance, 242 (2014) 4-9.

[32] X. Jiang, H. Li, J. Xie, P. Zhao, J.C. Gore, J. Xu, Quantification of cell size using temporal diffusion spectroscopy, Magnetic resonance in medicine, 75 (2016) 1076-1085.

[33] J. Xu, M.D. Does, J.C. Gore, Quantitative characterization of tissue microstructure with temporal diffusion spectroscopy, Journal of magnetic resonance, 200 (2009) 189-197.

[34] J. Keeler, Understanding NMR spectroscopy, John Wiley & Sons, 2010.

[35] V.J. Witherspoon, J. Xu, J.A. Reimer, Solid-state NMR investigations of carbon dioxide gas in metal–organic frameworks: insights into molecular motion and adsorptive behavior, Chemical reviews, 118 (2018) 10033-10048.

[36] R. Konrat, NMR contributions to structural dynamics studies of intrinsically disordered proteins, Journal of Magnetic Resonance, 241 (2014) 74-85.

[37] R. Borrego-Varillas, A. Nenov, L. Ganzer, A. Oriana, C. Manzoni, A. Tolomelli, I. Rivalta, S. Mukamel, M. Garavelli, G. Cerullo, Two-dimensional UV spectroscopy: a new insight into the structure and dynamics of biomolecules, Chemical Science, 10 (2019) 9907-9921.

[38] C. Westbrook, J. Talbot, MRI in Practice, John Wiley & Sons, 2018.

[39] G. Katti, S.A. Ara, A. Shireen, Magnetic resonance imaging (MRI)–A review, International journal of dental clinics, 3 (2011) 65-70.

[40] F. Bloch, Nuclear induction, Physical review, 70 (1946) 460.

[41] J.P. de Almeida Martins, D. Topgaard, Two-dimensional correlation of isotropic and directional diffusion using NMR, Physical review letters, 116 (2016) 087601.

[42] M.H. Levitt, Spin dynamics: basics of nuclear magnetic resonance, John Wiley & Sons, 2013.

[43] J. Pule, The Bloch equations, Communications in Mathematical Physics, 38 (1974) 241-256.

[44] E.L. Hahn, Spin echoes, Physical review, 80 (1950) 580.

[45] H. Lundell, S. Lasič, Diffusion encoding with general gradient waveforms, Advanced Diffusion Encoding Methods in MRI, 24 (2020) 12.

[46] H.C. Torrey, Bloch equations with diffusion terms, Physical review, 104 (1956) 563.

[47] B. Jian, B.C. Vemuri, E. Özarslan, P.R. Carney, T.H. Mareci, A novel tensor distribution model for the diffusion-weighted MR signal, NeuroImage, 37 (2007) 164-176.

[48] A. Arbabi, J. Kai, A.R. Khan, C.A. Baron, Diffusion dispersion imaging: mapping oscillating gradient spin-echo frequency dependence in the human brain, Magnetic resonance in medicine, 83 (2020) 2197-2208.

[49] P. Basser, J. Mattiello, D. Le Bihan, Estimation of the effective self-diffusion tensor from the NMR spin echo, J. Magn. Resort. B, 103 (1994) 247.

[50] P.B. Kingsley, Introduction to diffusion tensor imaging mathematics: Part II. Anisotropy, diffusion-weighting factors, and gradient encoding schemes, Concepts in Magnetic Resonance Part A, 28 (2006) 123-154.

[51] S. Eriksson, S. Lasič, M. Nilsson, C.-F. Westin, D. Topgaard, NMR diffusion-encoding with axial symmetry and variable anisotropy: Distinguishing between prolate and oblate microscopic diffusion tensors with unknown orientation distribution, The Journal of chemical physics, 142 (2015).

[52] H. Ulrich, High resolution NMR in solids: selective averaging, (No Title), (1976).

[53] D. Topgaard, Multiple dimensions for random walks, Journal of Magnetic Resonance, 306 (2019) 150-154.

[54] H. Lundell, M. Nilsson, T. Dyrby, G. Parker, P.H. Cristinacce, F.-L. Zhou, D. Topgaard, S. Lasič, Multidimensional diffusion MRI with spectrally modulated gradients reveals unprecedented microstructural detail, Scientific reports, 9 (2019) 9026.

[55] K. Holmberg, B. Jönsson, B. Kronberg, B. Lindman, Surfactants and Polymers in aqueous solution, Wiley-Blackwell, (2002).

[56] O. Söderman, P. Stilbs, W.S. Price, NMR studies of surfactants, Concepts in Magnetic Resonance Part A: An Educational Journal, 23 (2004) 121-135.

[57] D. Topgaard, Director orientations in lyotropic liquid crystals: diffusion MRI mapping of the Saupe order tensor, Physical Chemistry Chemical Physics, 18 (2016) 8545-8553.

[58] A. Khan, K. Fontell, G. Lindblom, B. Lindman, Liquid crystallinity in a calcium surfactant system. Phase equilibriums and phase structures in the system calcium octyl sulfate/decan-1-ol/water, The Journal of Physical Chemistry, 86 (1982) 4266-4271.

[59] J. Kneipp, https://fakultaeten.hu-berlin.de/en/mnf/forschung_internationales/grs/salsa/p-a-labs/application-lab/instrumentation/a-labs-lm/polarized-light-microscopy, in.

[60] Q. Liang, P. Liu, C. Liu, X. Jian, D. Hong, Y. Li, Synthesis and properties of lyotropic liquid crystalline copolyamides containing phthalazinone moiety and ether linkages, Polymer, 46 (2005) 6258-6265.

[61] T.M. Ferreira, D. Bernin, D. Topgaard, NMR studies of nonionic surfactants, Annual reports on NMR spectroscopy, 79 (2013) 73-127.

[62] R. Struis, J. De Bleijser, J. Leyte, Dynamic behavior and some of the molecular properties of water molecules in pure water and in magnesium chloride solutions, Journal of Physical Chemistry, 91 (1987) 1639-1645.

[63] J.E. Tanner, E.O. Stejskal, Restricted self-diffusion of protons in colloidal systems by the pulsed-gradient, spin-echo method, The Journal of Chemical Physics, 49 (1968) 1768-1777.

[64] Y. Cheng, D.G. Cory, Multiple scattering by NMR, Journal of the American Chemical Society, 121 (1999) 7935-7936.

[65] S. Lasič, F. Szczepankiewicz, S. Eriksson, M. Nilsson, D. Topgaard, Microanisotropy imaging: quantification of microscopic diffusion anisotropy and orientational order parameter by diffusion MRI with magic-angle spinning of the q-vector, Frontiers in Physics, 2 (2014) 11.

[66] J.P. de Almeida Martins, D. Topgaard, Multidimensional correlation of nuclear relaxation rates and diffusion tensors for model-free investigations of heterogeneous anisotropic porous materials, Scientific reports, 8 (2018) 2488.

[67] L. Wadsö, A. Anderberg, I. Åslund, O. Söderman, An improved method to validate the relative humidity generation in sorption balances, European journal of pharmaceutics and biopharmaceutics, 72 (2009) 99-104.

[68] D.-H. Kim, H. Zeng, T.C. Ng, C.S. Brazel, T1 and T2 relaxivities of succimer-coated MFe23+ O4 (M= Mn2+, Fe2+ and Co2+) inverse spinel ferrites for potential use as phase-contrast agents in medical MRI, Journal of Magnetism and Magnetic Materials, 321 (2009) 3899-3904.

[69] A. Reymbaut, Y. Zheng, S. Li, W. Sun, H. Xu, I. Daimiel Naranjo, S. Thakur, K. Pinker-Domenig, S. Rajan, V. Vanugopal, Clinical research with advanced diffusion encoding methods in MRI, New Developments in NMR, 2020 (2020) 406-429.

[70] S. Eriksson, S. Lasic, D. Topgaard, Isotropic diffusion weighting in PGSE NMR by magic-angle spinning of the q-vector, Journal of Magnetic Resonance, 226 (2013) 13-18.

[71] D. Topgaard, Isotropic diffusion weighting in PGSE NMR: numerical optimization of the q-MAS PGSE sequence, Microporous and Mesoporous Materials, 178 (2013) 60-63.

[72] I. Åslund, D. Topgaard, Determination of the self-diffusion coefficient of intracellular water using PGSE NMR with variable gradient pulse length, Journal of Magnetic Resonance, 201 (2009) 250-254.

[73] G. Lipari, A. Szabo, Model-free approach to the interpretation of nuclear magnetic resonance relaxation in macromolecules. 1. Theory and range of validity, Journal of the American Chemical Society, 104 (1982) 4546-4559.

[74] D. Topgaard, Diffusion tensor distribution imaging, NMR in Biomedicine, 32 (2019) e4066.

[75] M. Prange, Y.-Q. Song, Quantifying uncertainty in NMR T2 spectra using Monte Carlo inversion, Journal of Magnetic Resonance, 196 (2009) 54-60.

[76] I. Åslund, A. Nowacka, M. Nilsson, D. Topgaard, Filter-exchange PGSE NMR determination of cell membrane permeability, Journal of Magnetic Resonance, 200 (2009) 291-295.

[77] A. Romiani, J. Spetz, E. Shubbar, D.E. Lind, B. Hallberg, R.H. Palmer, E. Forssell-Aronsson, Neuroblastoma xenograft models demonstrate the therapeutic potential of 177Lu-octreotate, BMC cancer, 21 (2021) 1-14.

[78] M. Yon, J.P. de Almeida Martins, Q. Bao, M.D. Budde, L. Frydman, D. Topgaard, Diffusion tensor distribution imaging of an in vivo mouse brain at ultrahigh magnetic field by spatiotemporal encoding, NMR in Biomedicine, 33 (2020) e4355.

[79] M. Aggarwal, M.V. Jones, P.A. Calabresi, S. Mori, J. Zhang, Probing mouse brain microstructure using oscillating gradient diffusion MRI, Magnetic resonance in medicine, 67 (2012) 98-109.

[80] K.D. Harkins, C. Beaulieu, J. Xu, J.C. Gore, M.D. Does, A simple estimate of axon size with diffusion MRI, Neuroimage, 227 (2021) 117619.

Printed by Media-Tryck, Lund 2023 NORDIC SWAN ECOLABEL 3041 0903

ISBN 978-91-7422-978-3

Physical Chemistry
Faculty of Science
Lund University